Reactive soil inputs during high-flow events decouple carbon chemistry and CO_2 evasion in a granitic headwater stream

Christina M. Schubert[a]*, Robert van Geldern[a], Harald Maid[b], Christian Placht[b], Marcus Speck[b], Johannes A. C. Barth[a] and Anna-Neva Visser[a]

[a]*Friedrich-Alexander-Universität Erlangen-Nürnberg, Geozentrum Nordbayern, Department Geographie und Geowissenschaften, Schlossgarten 5, 91054 Erlangen, Germany*

[b]*Friedrich-Alexander-Universität Erlangen-Nürnberg, Department of Chemistry and Pharmacy, Nikolaus-Fiebiger Straße 10, 91058 Erlangen, Germany*

Corresponding author: CMS: 0000-0001-8048-7338, email: christina.cs.schubert@fau.de

RvG: 0000-0003-2786-2893, email: robert.van.geldern@fau.de

HM: email: harald.maid@fau.de

CP: email: christian.placht@fau.de

MS: 0000-0003-4186-8669, email: marcus.speck@fau.de

JACB: 0000-0002-3494-4507, email: johannes.barth@fau.de

ANV: 0000-0002-8447-5825, email: anna-neva.visser@fau.de

This manuscript is a non-peer-reviewed preprint submitted to EarthArXiv.

The manuscript is currently being revised for resubmission to Environmental Science & Technology.

ABSTRACT: Quantifying CO_2 dynamics in low-alkalinity headwater streams is challenging because thermodynamically based evaluations of pCO_2 and CO_2 fluxes (F_{CO2}) assume coherent DIC-alkalinity-pH coupling. This study examines how hydrologically driven disturbances violate this assumption in a forested, granitic headwater stream using 15 months of calculated pCO_2 and F_{CO2}, alongside measurements of pH, alkalinity, dissolved inorganic and organic carbon (DIC, DOC, $\delta^{13}C_{DIC}$, $\delta^{13}C_{DOC}$), major ion chemistry, redox-sensitive metals, and natural organic matter characterization ($SUVA_{254}$, ^{13}C-NMR). During baseflow, pCO_2 declined sharply from the spring (~11 088 µatm) to downstream sites, approaching atmospheric levels. In contrast, high-flow events produced large increases in pCO_2 and F_{CO2} (up to 4.5-fold downstream), accompanied by decreases in $\delta^{13}C_{DIC}$ (2-4‰), pH (up to 0.9 units), and alkalinity (up to 0.01 mmol L^{-1}), elevated DOC, and enhanced mobilization of Fe, Al, and Mn, while measured DIC showed no proportional increase. Charge-balance errors exceeding –20 % during these events indicate contributions of unquantified proton-active solutes. Soil mineralogical analyses and NOM extractions revealed organic functional groups and fine minerals consistent with these perturbations. Together, these results demonstrate that high-flow mobilization of soil-derived organic and inorganic species decouples DIC-alkalinity-pH dynamics, systematically biasing thermodynamically based pCO_2 and F_{CO2} evaluations in weakly buffered granitic streams.

1. Introduction

Inland waters are increasingly recognized as dynamic components of the global carbon cycle, acting both as conduits that transport terrestrial carbon (C) and as biochemical reactors that process and emit substantial amounts of carbon dioxide (CO_2) to the atmosphere (Aufdenkampe et al., 2011; Cole et al., 2007; Lauerwald et al., 2023; Marx et al., 2017; Raymond et al., 2013). Headwater streams in particular constitute more than 90% of the global river network length and contribute disproportionately to riverine CO_2 emissions (Marx et al., 2017) due to their short hydrological residence times, steep gradients and efficient air–water gas exchange (Chan et al., 2021; Kokic et al., 2018; Marx et al., 2017). As such small, hydrologically dynamic systems have been progressively incorporated into global assessments, determined riverine CO_2 emissions have increased from ~0.8 Pg C $year^{-1}$ (Cole et al., 2007) to values exceeding 4 petagram (Pg) C $year^{-1}$ (Pilla et al., 2022). Despite this growing recognition, the mechanisms controlling CO_2 variability in headwater networks remain insufficiently constrained, particularly at finer spatial and temporal scales.

A central methodological challenge in quantifying CO_2 dynamics in headwater systems arises from the common practice of calculating CO_2 partial pressure (pCO_2) and CO_2 flux (F_{CO2}) from pH, alkalinity, and temperature under the assumption of coherent DIC-system behavior and closed proton budgets (Herrmann et al., 2020; Hope et al., 1995; Raymond and Cole, 2001). However, headwaters frequently experience variable deviations in proton balance (Demers et al., 2010; Winnick and Saccardi, 2024), redox potentials (Abesser et al., 2006; Riise et al., 2023), groundwater contributions and in-stream CO_2 production (Björnerås et al., 2019; Duvert et al., 2018; Johnson et al., 2008), all of which can transiently decouple DIC speciation, alkalinity, and pH, violating the assumptions of coherent carbon-system behavior. Even small perturbations in pH or alkalinity may translate into orders-of-magnitude differences in calculated pCO_2, raising concerns about the robustness of thermodynamically based flux

calculations in low-alkalinity environments (Abril et al., 2015; Clow et al., 2021; Dawson et al., 2001; Herrmann et al., 2020). This issue is amplified in high-gradient catchments where turbulence enhances gas exchange and rapid shifts in water-soil connectivity during rainfall or snowmelt promote strong biogeochemical turnover (Attermeyer et al., 2018; Duvert et al., 2018; McCallister et al., 2018; Norwood et al., 2023). Yet, most studies quantify pCO_2 and F_{CO2} at kilometer-scale intervals, leaving a critical data gap in the first meters downstream of the spring, where disequilibria are most pronounced (Marx et al., 2017; Öquist et al., 2009; van Geldern et al., 2015).

Forested, granitic headwater catchments represent an extreme expression of this sensitivity. Their silicate-dominated lithology produces dilute waters with minimal carbonate buffering, while thin, organic-rich soils respond rapidly to hydrological forcing (Adler et al., 2021; Schimmel et al., 2025; Zhang and Furman, 2021). During high-flow events, shallow soil horizons become hydrologically connected to the stream, delivering waters enriched in proton-active dissolved and particulate natural organic matter (NOM), reduced species, trace metals and fine mineral phases (Burger et al., 2021; Cincotta et al., 2019; Demers et al., 2010). Such inputs can alter proton budgets, induce non-carbonate alkalinity, or influence metal-organic complexation, potentially biasing DIC-alkalinity-pH based interpretations (Nayna et al., 2021). Yet, whether these event-driven soil inputs are sufficiently strong to cause detectable deviations from these assumptions in weakly buffered streams remains poorly constrained.

These short-term hydrological perturbations are expected to intensify under future climate conditions due to shifts in precipitation patterns, runoff extremes and snowmelt dynamics (Battin et al., 2009; Carter et al., 2022; Knutson et al., 2021). Concurrently, widespread brownification across many northern and temperate regions highlights the growing influence of terrestrial organic C export on surface-water chemistry (Haaland et al., 2024; Kritzberg and Ekström, 2012; Škerlep et al., 2022). Together, these trends emphasize a broader

methodological issue: short-lived soil-stream reconnection might transiently reshape the dominance of DIC speciation in low-buffered headwaters, thereby compromising thermodynamically based pCO_2 and F_{CO2} calculations. Whether such chemically mediated shifts are sufficiently large to alter flux interpretations at the reach scale, however, remains uncertain.

To investigate this gap, a high-gradient, forested granitic headwater stream, characterized by short-term high-discharge events and strong soil-stream connectivity, was investigated over 15 months. A spatially resolved multi-tracer dataset combining CO_2/DIC system metrics (pCO_2, F_{CO2}, $\delta^{13}C_{DIC}$, $\delta^{13}C_{DOC}$), hydrochemistry, redox-sensitive elements, mineral interactions and NOM inputs was used to identify the dominant controls on transient CO_2 variability. Given the pronounced chemical sensitivity of this weakly buffered system, three mechanisms were evaluated as potential mechanisms contributing to observed deviations:

(i) Rapid shifts in pH, alkalinity and non-carbonate proton sources during high flow may disrupt the internal coherence between pH, alkalinity and DIC, rendering thermodynamically based calculations of pCO_2 and F_{CO2} potentially unreliable.

(ii) Mobilization of clay-associated ions and mineral colloids during high flow may induce charge-balance deviations and apparent alkalinity shifts, thereby biasing the interpretation of pH and alkalinity without proportional changes in measured dissolved inorganic carbon.

(iii) Mobilization of proton-active NOM during soil-stream reconnection may introduce non-carbonate alkalinity and reduce the relative contribution of carbonate alkalinity, biasing reconstructed pCO_2 and F_{CO2} values and potentially mimicking hydrologically driven CO_2 production.

By linking soil-derived inputs to instream DIC-alkalinity-pH dynamics, this study provides mechanistic insights into how hydrological pulses govern CO_2 fluxes and C cycling in low-buffered headwater streams.

2. Material and Methods

2.1 Field site and sampling design

Sampling was conducted along the first 1.5 km of the White Main headwater stream, a steep, forested catchment in the Fichtelgebirge (northern Bavaria; Germany, Figure 1). The silicate-dominated lithology and thin acidic soils result in dilute stream water and low buffering capacity (Bayerisches Landesamt für Umwelt, 2024).

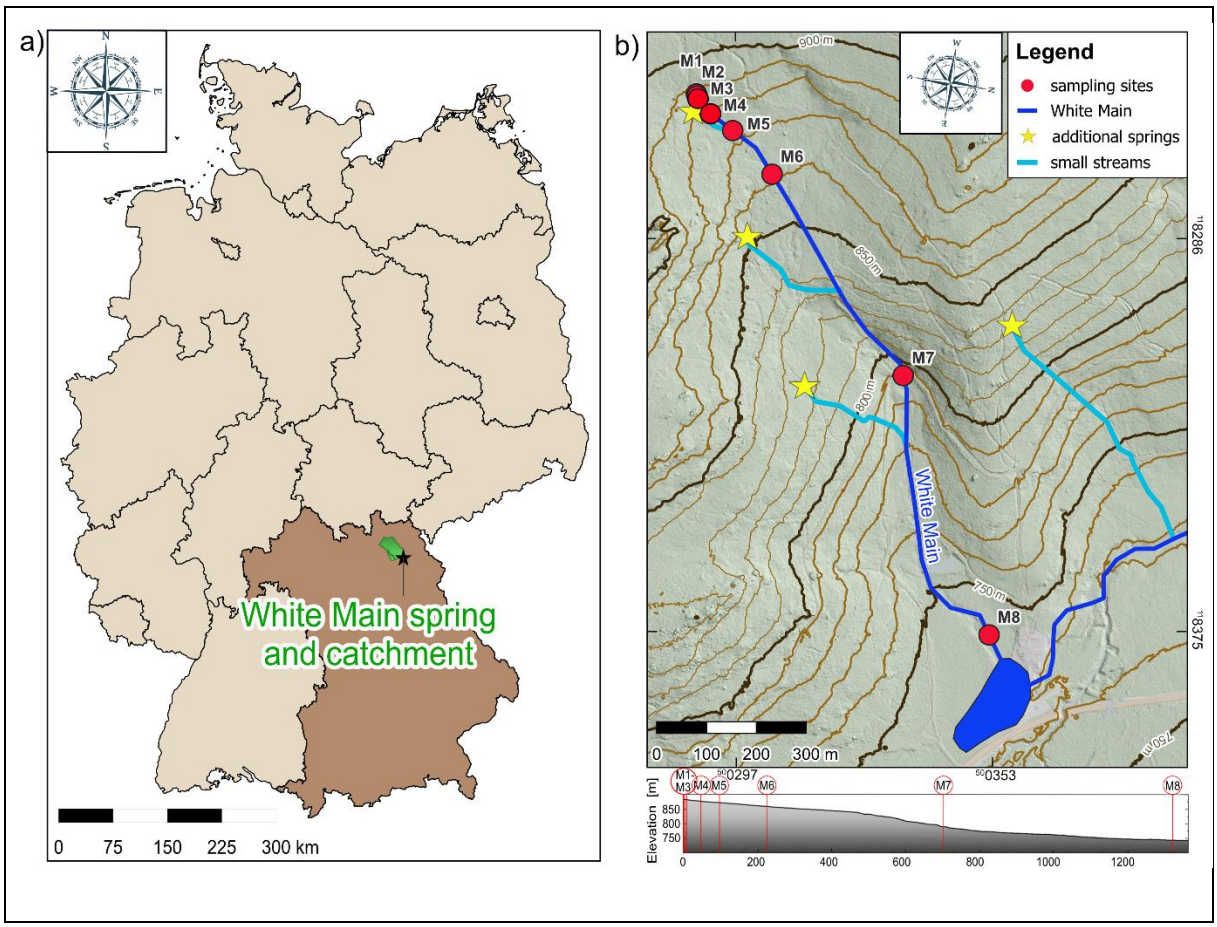

***Figure 1**: a) Location of the White Main catchment (green) and spring (black star) in Bavaria (dark brown), Germany. b) Topographic map of the White Main headwater catchment (Gauß-Krüger Zone 4 coordinate system) showing the stream course (dark blue), sampling sites (M1-M8, red dots), additional*

springs (yellow stars); tributaries (light blue lines), elevation contours (brown lines) and a longitudinal profile of the first 1500 m. Source: Bayerische Vermessungsverwaltung (https://geodaten.bayern.de/opengeodata/, accessed: 15.03.2024).

Eight sampling locations (M1-M8) were selected from the spring source to downstream reaches to capture spatial hydrochemical gradients (Figure 1 b, Table 1). Fifteen monthly sampling campaigns (March 2023-May 2024) were performed under both baseflow and high-flow conditions. Baseflow discharge averaged ~0.39 $m^3 s^{-1}$ at a downstream gauging station (Bad Berneck; Bayerisches Landesamt für Umwelt, 2025), which was used as a proxy for high-flow vs baseflow classification along the upstream sampling transect. High-flow events occurred in August 2023 and from November 2023 to January 2024, peaking at ~10.8 $m^3 s^{-1}$ in December. Total precipitation during the study period was 1898 mm (weather station Bischofsgrün; DWD Climate Data Center (CDC), 2025), consistent with the humid climate of the Fichtelgebirge (Supporting information (SI) B , Figure S1).

***Table 1**: Overview of all sampling locations along the White Main headwater transect, including geographic coordinates (latitude and longitude), elevation (m a. s. l.), and distance from the spring (m).*

Sample ID	LAT [N°]	LON [E°]	Elevation [m a. s. l.]	Distance to spring [m]
M1*	50.02987	11.82367	886	0
M2	50.02988	11.82373	886	4
M3	50.02991	11.82381	885	11
M4	50.03017	11.82416	879	50
M5	50.03061	11.82454	873	106
M6	50.03142	11.82562	860	226
M7	50.03426	11.83074	790	715
M8	50.03645	11.83765	743	1310

*spring

In situ measurements included temperature, pH, electrical conductivity (EC), and redox potential (Eh), measured with a calibrated Multi 350i instrument (WTW GmbH, Weilheim,

Germany). Stream water was collected mid-channel, filtered (0.45 µm) and stored at 4 °C in the dark. Alkalinity samples were collected unfiltered in crimp-top glass bottles for laboratory titration (CS-Chromatographie Service GmbH, Langerwehe, Germany). Samples for DIC, DOC and their $\delta^{13}C$ isotopes were collected in amber borosilicate vials with butyl rubber septa, while major ion samples were stored in 15 mL Falcon tubes (BD Biosciences, Bedford, USA). Discharge was measured in triplicates at each site using bucket-and-stopwatch gauging and, at M8, with an impeller (Schubert et al., 2026). Further details are provided in SI A, S1.

2.2 Characterization of C system dynamics

To evaluate carbon dynamics along the White Main transect, total alkalinity (TA), dissolved inorganic carbon concentrations (c(DIC)) and their stable isotope ratios ($\delta^{13}C_{DIC}$) were measured in the laboratory, whereas pCO_2 and F_{CO2} were calculated. Analytical details are provided in SI A, S2-S5.

TA was determined in triplicates by automated acid titration (Eco Titrando, Metrohm AG, Herisau, Switzerland), with inflection point detection (Rounds and Wilde, 2012), yielding a precision of <0.03 mmol L^{-1}. Given the granitic lithology and low ionic strength, TA was treated as a first-order approximation of carbonate alkalinity at pH values <7, an assumption explicitly evaluated in this study.

$\delta^{13}C_{DIC}$ and c(DIC) were analysed in triplicates using an automated equilibration unit coupled to a Delta *plus* XP isotope ratio mass spectrometer (IRMS) (Thermo Fisher Scientific, Bremen, Germany). All isotope values are reported in standard permille-notation (‰) versus the Vienna Pee Dee Belemnite (VPDB) according to:

$$\delta^{13}C = \left(\frac{R_{Sample}}{R_{Reference}} - 1\right) \quad (1)$$

where R is the ratio of the numbers (n) of the heavy and light isotope of an element (i.e., $n(^{13}C)/n(^{12}C)$) in the sample and the reference (Coplen 2011). To account for instrumental drift and linearity, data correction was applied. $\delta^{13}C_{DIC}$ precision generally remained within ± 0.3 ‰ (1-σ). DIC concentrations were calculated from peak areas with <5% precision. Further details can be viewed in Schubert et al. (2023).

pCO_2 was calculated from temperature, pH values and TA using standard carbonate-equilibrium formulations (Marx et al., 2017; Plummer and Busenberg, 1982). Under freshwater conditions, pCO_2 approximates CO_2 fugacity within <1% (Dickson et al., 2007). CO_2 fluxes (F_{CO2}) were computed as:

$$F_{CO2} = k \times ([CO_2^*] - [CO_{2_{air}}]) \quad (2)$$

with k as the gas transfer velocity, determined from site specific stream hydraulics, and the concentrations of dissolved CO_2 in the stream water $[CO_2^*]$ and in the water at equilibrium with the overlaying atmosphere $[CO_{2air}]$ (Raymond et al., 2012; Schubert et al., 2023; van Geldern et al., 2015).

2.3 Major ions and trace elements

Major cations and trace elements were quantified by ICP-MS (iCAP Qc, Thermo Fisher Scientific Inc., Bremen, Germany, 1σ-precision <1 %) and major anions via ion chromatography (Compact IC Flex, Metrohm, Herisau, Switzerland, 1σ-precision <5 %). (SI A, S6). Analytical consistency was assessed using the charge balance error (CBE) for major ions, selected trace elements (e.g. Al, Mn, Fe) and DOC. Values within ±5 %, and up to ±10 % in low-ionic-strength waters, were considered acceptable (SI A, S7; Appelo and Postma, 2004; Fritz, 1994).

2.4 Mineralogical and colloidal characterization

Composite soil samples (M4, M6, M8 (I-III)), SI A, S8) were analyzed to characterize mineral phases potentially mobilized during high flow. Mineralogy was determined by X-ray diffraction (XRD, Siemens D5000), utilizing a Cu-long-fine-focus tube (Cu-Kα wavelength of 1.5406 Å) with a standard scintillation detector (scan range of 2 to 65° 2θ), and semi-quantitative Rietveld refinement (SI A, S9; Doebelin and Kleeberg, 2015). Particle size distributions were measured to evaluate clay-sized fractions after dispersion and wet-sieving (Sedigraph III Plus 5125 coupled to a MasterTech autosampler; SI A, S10). Saturation indices (SI) for relevant mineral phases were calculated using PHREEQC (version 3.7.3, Parkhurst (1995)) with the Thermoddem database (V1.10, French geological survey) to assess mineral dissolution (SI<0) or precipitation (SI>0) tendencies based on pH, temperature, TA, major ions and selected trace elements. These calculations provide thermodynamic context but do not quantify dissolution rates. Colloidal surface-charge behavior under stream-relevant conditions was assessed via zeta-potential (ζ), a measure of colloidal surface charge and electrostatic stability, using soil-derived suspensions in Milli-Q water (pH 6.3, from an in-house ultrapure water system) and White Main water adjusted to pH 5.0 to simulate baseflow and high-flow conditions with a ZetaView instrument (Particle Metrix GmbH, Inning, Germany, software version 8.0516 SP3; SI A, S11). These analyses indicate relative colloid stability/aggregation but do not represent in-stream colloid concentrations (He et al., 2021; Hunter, 1981).

2.5 Organic matter analyses

DOC concentrations and $\delta^{13}C_{DOC}$ were measured using a coupled OI Analytical Aurora 1030W TIC-TOC analyzer (OI Analytical, College Station, Texas) coupled to a Thermo Scientific Delta V plus IRMS. Analytical precision (1σ) was <0.3 ‰ for $\delta^{13}C_{DOC}$ and <5 % for DOC concentrations (SI A, S3). To qualitatively assess functional groups in soil-derived organic

matter potentially mobilized during high flow, simplified NOM extractions were performed (B1) following a modified acid-base extraction protocol (Krivdin, 2024), based on the IHSS extraction procedure (International Humic Substances Society, 2024; Swift, 1996), and (B2) a mild extraction with White Main water to approximate *in situ* mobilization (SI A, S12). Specific ultraviolet absorbance at 254 nm ($SUVA_{254}$) was determined by UV-VIS spectroscopy (Tecan Infinite 200Pro) to determine the aromaticity indices of these soil extracts (Levchuk et al., 2018; Weishaar et al., 2003) following established blank and pathlength corrections (Potter and Wimsatt, 2005; Weishaar et al., 2003; SI A, S13).

As DOC concentrations in stream water were insufficient for NMR analysis, ^{1}H- and ^{13}C-NMR spectra were obtained from soil-extract fractions using a Bruker 600 MHz Avance NEO spectrometer equipped with a cryoprobe (CPDCH600S3 C/H-D-05Z). The spectra were used for qualitative assessment of aromatic, aliphatic and carboxyl carbon functional groups and are not intended to represent in-stream dissolved NOM composition. A Pahokee Peat Humic Acid standard (PPHA; 1S103H) served as reference. Acquisition parameters followed Kaiser (2003) and are provided in SI A, S14.

2.6 Statistics

Principal Component Analysis (PCA) was applied to z-standardized datasets to evaluate multivariate ion chemistry patterns in ion chemistry (chapter 3.2) and soil suspension properties (chapter 2.4) using the *prcomp* function in R, version 4.3.2 (R Core Team Vienna, 2023)

Group comparisons between suspensions in Milli-Q vs White Main water, as well as between clay-influenced samples (M8-III) and other sites, were evaluated for normality (Shapiro and Wilk, 1965) and homogeneity (Levene, 1960). ANOVA was used when assumptions were met (Fisher, 1992), Wilcoxon when they were violated (Wilcoxon, 1945). A significance level of $p < 0.05$ was applied.

3. Results

3.1 Carbon-system dynamics under baseflow and high-flow conditions

All carbon system parameters exhibited pronounced spatial gradients and temporal variability along the 1.5 km transect (Figure 2 a-f). During baseflow, pCO_2 was highest at M1 with values up to 16 248 µatm and declined consistently downstream, reaching values near atmospheric equilibrium (~420 µatm) at M6-M8 (Figure 2 a). F_{CO2} followed the same pattern, decreasing from max. 99 000 mmol m^{-2} d^{-1} at the M1 to −5 100 mmol m^{-2} d^{-1} at M8 (Figure 2 b). These downstream declines coincided with pH increases from ~5.19 to ~7.28 units (Figure 2 c), constantly low alkalinity, ranging around 0.04±0.01 mmol L^{-1} across all sites (Figure 2 d) and decreasing c(DIC) values from max. 0.62 mmol L^{-1} to min. 0.02 mmol L^{-1} (Figure 2 e). Concomitantly, $\delta^{13}C_{DIC}$ values rose from −25.1 ‰ to −4.6 ‰, respectively (Figure 2 f). Between M7 and M8, these trends partially reversed, with modest increases in pCO_2, F_{CO2}, and c(DIC), and small decreases in pH, and a depletion in $\delta^{13}C_{DIC}$ values.

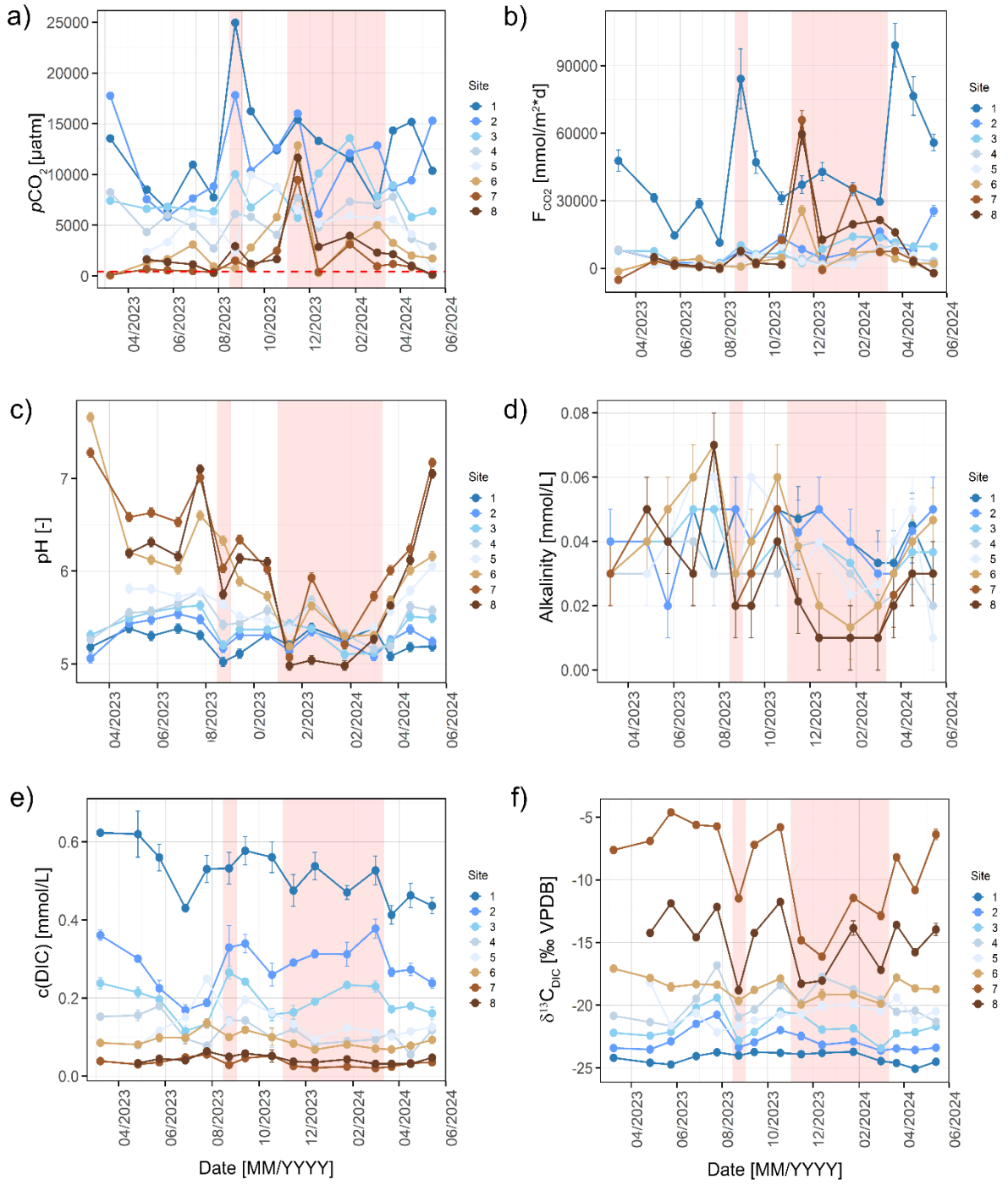

Figure 2: Temporal and spatial variation of carbon-system parameters along the White Main transect (March 2023-May 2024): a) aqueous partial pressure (pCO_2, µatm), b) CO_2 fluxes (F_{CO2}, mmol m^{-2}), c) pH [-], d) alkalinity [mmol L^{-1}], e) dissolved inorganic carbon concentrations (c(DIC), mmol L^{-1}), and f) $\delta^{13}C_{DIC}$ isotopes [‰ VPDB]. Red shading indicates high flow (SI B, Figure S1). Symbols represent mean values.

High-flow events, identified from SI B, Figure S1, produced substantial positive deviations from this baseflow pattern. Across events in August and from November till January, pCO_2 increased at all sites, most strongly at locations M7-M8, where values were elevated by 4.5-

fold (Figure 2 a). Correspondingly F_{CO2} rose from near-background levels to pronounced maximum peaks of 65 900 mmol m^{-2} d^{-1} at those downstream sites during both events (Figure 2 b). Despite these temporal fluctuations, the spatial structure of the transect remained consistent: Spring-proximal sites (M1-M3) showed persistently elevated pCO_2 and F_{CO2} values, sites M4-M5 formed a transitional zone, and downstream sites (M6-M8) expressed the highest responsivity towards high-flow events. The increases in pCO_2 and F_{CO2} at M7 and M8 during high flow coincided with distinct decreases in pH and alkalinity, reaching minimum values of 5.0 units and 0.01 mmol L^{-1} at site M8 (Figure 2 c, d). In contrast c(DIC) remained similar to baseflow, while $\delta^{13}C_{DIC}$ decreased by 2-4 ‰ at M7-M8 relative to baseflow were detected (Figure 2 e, f).

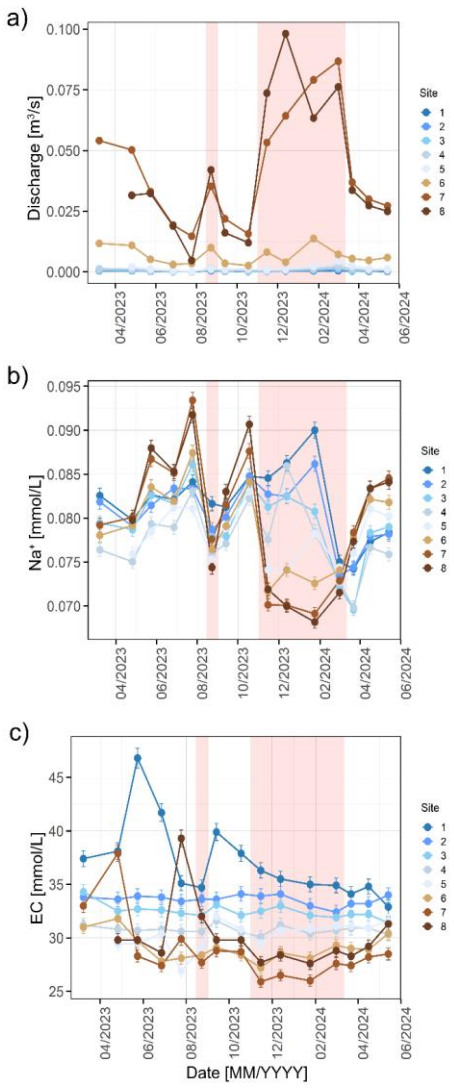

Figure 3: Temporal and spatial variation of a) discharge [$m^3 s^{-1}$], b) Na^+ concentration (mmol L^{-1}), and EC (mmol L^{-1}) along the sampling transect (March 2023-May 2024). Red shading shows high-flow times.

Discharge increased from min. 7.21×10^{-5} m^3 s^{-1} to max. 5.41×10^{-2} m^3 s^{-1} during baseflow and reached up to 9.81×10^{-2} m^3 s^{-1} during high flow (Figure 3 a). Na^+ remained low and only varied in a narrow range around 0.081 ±0.004 mmol L^{-1}, whereas EC declined from 46.8 µS cm^{-1} at M1 to 28.3 µS cm^{-1} at M8 (Figure 3 b, c). High flow induced only small Na^+ decreases (min. 0.068 mmol L^{-1}) and minor EC reductions of 1-2 µS cm^{-1}. Comparable trends were observed for Cl^-, SO_4^{2-} and NO_3^- (SI B, Figure S3, which together span conservative (Cl^-) to conditionally reactive (SO_4^{2-} and NO_3^-) behavior and indicate a dominant influence of hydrological dilution and mixing processes. As pH-alkalinity-DIC relationships showed clear

changes during high flow, we next examined whether corresponding variations occurred in the ionic charge balance and major/trace element chemistry.

3.2 Major ions, charge balance, and trace metals

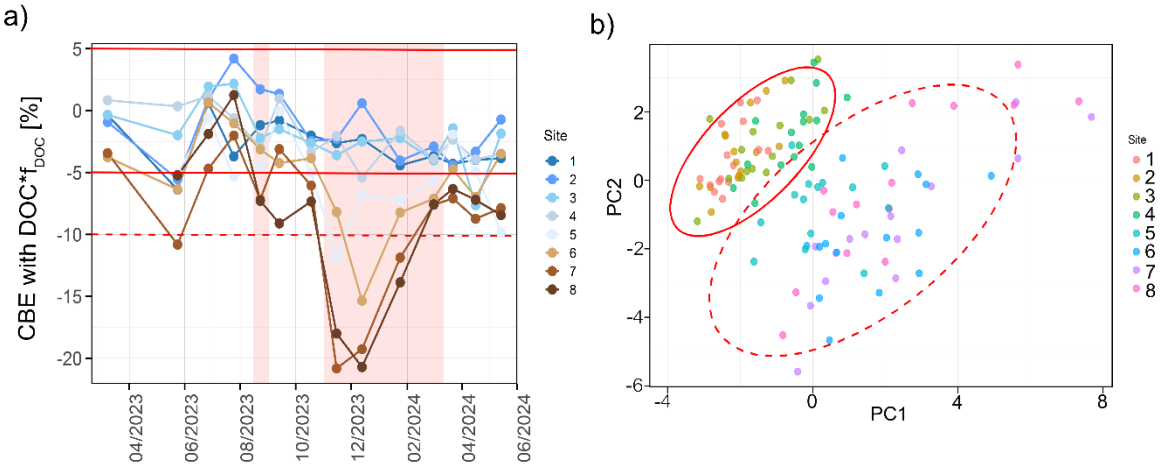

Figure 4: a) Temporal and spatial variability in charge balance errors (CBE) at the eight sampling sites (March 2023-May 2024). Red shadings indicate high flow. b) PCA of major ions and trace elements across all sites and sampling times (PC1 vs. PC2). Red ellipses highlight clustering of upstream and downstream samples.

Charge balance errors (CBEs) remained within ±5 % at upstream sites (M1-M4) during baseflow but increased downstream, up to ±10% at M6-M8 (Figure 4 a). During high-flow events, CBEs became strongly negative at downstream sites, exceeding -20% in November-December, with maximum deviations at M7-M8. PCA of major ions and trace elements (Figure 4 b) provided a multivariate summary of spatial and temporal variation across the transect. PC1 explained 32 %, and PC2 21 %, together accounting for 53 % of the total variance. Samples from upstream sites (M1-M4) clustered tightly, whereas downstream sites (M6-M8) were spread toward higher PC1 values and thus showed broader variability. Site M5 occupied an intermediate position between these groups. This pattern reflects the cumulative downstream increases in Fe, Al and Mn as well as changes in major-ion concentrations observed in Figure 3.

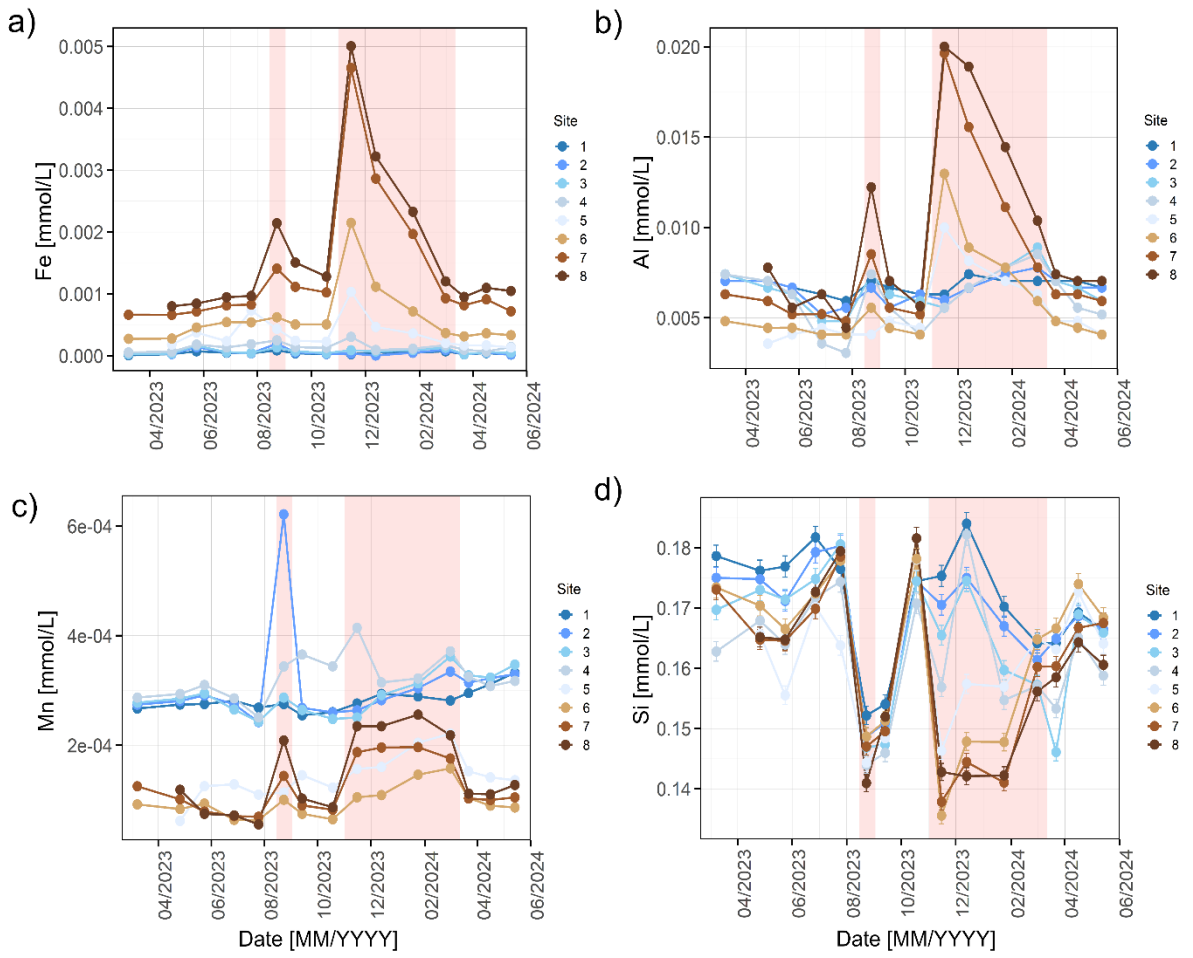

Figure 5: Temporal and spatial dynamics of a) iron (Fe), b) aluminum (Al), c) manganese (Mn), and d) silicium (Si) across the transect (March 2023-May 2024). Red shadings indicate high flow; error bars are smaller than symbol size for Fe, Al and Mn.

Trace metal concentration followed distinct spatial patterns (Figure 5). During baseflow, Fe and Al slightly increased downstream (Fe: 9.15×10^{-6} mmol L^{-1} to 1.5×10^{-3}mmol L^{-1}; Al: 4.08×10^{-5} mmol L^{-1} to 3.3×10^{-3} mmol L^{-1}), whereas Mn concentrations remained low and spatially uniform (Figure 5 a-c). High-flow events produced clear increases in Fe, Al and Mn at downstream sites, with November peaks at M7-M8 (Fe up to 5.01×10^{-3}; Al up to 2.00×10^{-2} mmol L^{-1}; Mn up to 2.56×10^{-4}). Silicon (Si) concentrations fluctuated throughout the year, yet remained relatively low and decreased slightly during high flow (from 0.17 ±0.01 mmol L^{-1} to 0.14 mmol L^{-1}, Figure 5 d). Redox potentials (Eh) ranged from 383 and 656 mV, with modest decreases at M6-M8 during high flow (SI B, Figure S5). To provide additional

context for the observed downstream variations in ion compositions and charge-balance behavior, we characterized soil mineralogy and clay-related properties.

3.3 Soil-mineral related interactions

The composite soil sample obtained from sites M4, M6 and M8I-III, exhibited a coarse texture, dominated by sand (74 %), with 22 % silt, and 4 % clay (Figure 6 a). XRD analysis identified quartz, K-feldspar and albite as primary mineral phases (~90 %), with chlorite and illite comprising the remaining ~10% (Figure 6 b).

PHREEQC-derived saturation indices for illite (SI) were slightly above equilibrium at upstream sites during baseflow, increasing modestly downstream (SI max. 10.5). During high-flow periods, SI values declined, with lowest values observed at site M8 between November and February, reaching values below zero (Figure 6 c). The soil-suspension PCA separated samples by water type (Milli-Q, pH 6.3 vs. White Main (WMQ) water, pH 5.0) and by sampling location (Figure 6 d). Across samples M4, M6 and M8I-II, ζ-potentials ranged between −24 and −13 mV, with pH decreasing consistently after 24 h of shaking, and no significant differences ($p > 0.05$) between suspensions. In contrast, the clay-enriched M8III sample exhibited less negative ζ-potentials (−2 to −3 mV) and significantly ($p<0.04$) smaller pH decreases. Statistical summaries are provided in SI B, Table S1. As mineralogical analyses revealed spatial differences in fine fractions and colloidal behavior, dissolved and soil-derived organic matter have been further assessed to complete the characterization of potential chemical constituents.

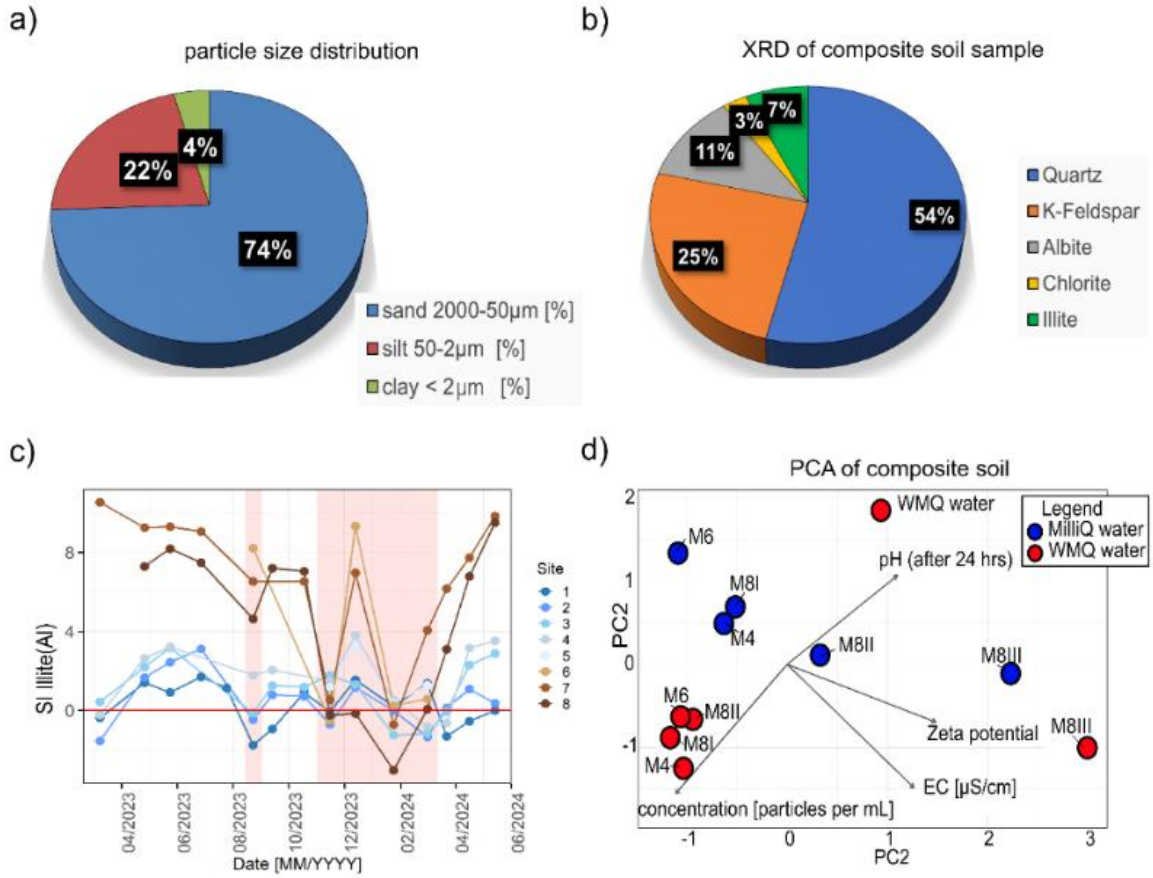

Figure 6: a) Particle size distribution of composite soils from the White Main (M4, M6 and M8). b) Mineral composition from X-ray diffraction (XRD) of the composite soil sample. c) Temporal and spatial evolution of saturation indices (SI) for illite (PHREEQC). d) PCA of composite soil suspensions in Milli-Q or White Main water (WMQ) showing the relationships between ζ-potential, pH, and ionic strength.

3.4 Dissolved organic carbon (DOC) and natural organic matter (NOM) characteristics

DOC concentrations remained low and stable at upstream sites during baseflow (0.11 ±0.02 mmol L^{-1}, M1-M4) and increased downstream up to 0.26 ±0.05 mmol L^{-1} (Figure 7 a). The accompanying $\delta^{13}C_{DOC}$ values remained near –28.1 ±0.1 ‰ (Figure 7 a, b), while $SUVA_{254}$ values ranged between 1.44 and 3.79 L mg^{-1} m^{-1} at sites M5 to M8 (Figure 7 c). High-flow periods produced sharp increases in DOC beginning at M5, with maximum values at M7-M8 in November (up to 1.26 mmol L^{-1}; roughly twice baseflow concentrations). At M7 and M8, $\delta^{13}C_{DOC}$ values exhibited a minor enrichment (max. –26.7 ‰) during these events (Figure 7 a,

b), whereas $SUVA_{254}$ aromaticity increased during autumn and early winter, with maxima in October and during high-flow months (up to >4 L mg^{-1} m^{-1} at M6-M7). $SUVA_{254}$ gradually decreased after February (Figure 7 c).

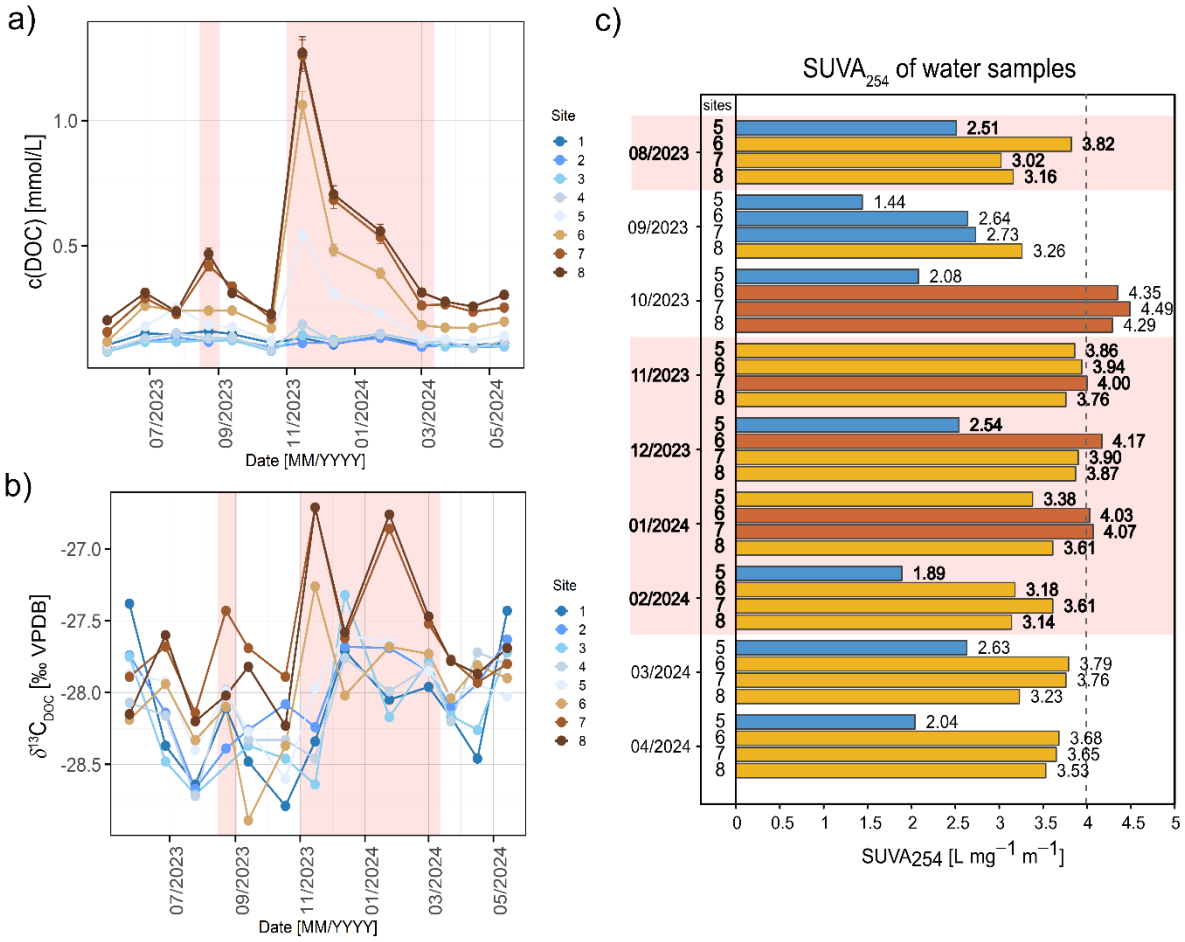

***Figure 7**: Spatial and temporal dynamics in a) dissolved organic carbon concentrations (c(DOC)) and b) $\delta^{13}C_{DOC}$ [‰ VPDB] across all sampling sites (June 2023-May 2024). c) $SUVA_{254nm}$ [L $mg^{-1}m^{-1}$] values of water samples from downstream sites (M5-M8, August 2023-April 2024). Blue values lie under 3 L $mg^{-1}m^{-1}$, yellow between 3-4 L $mg^{-1}m^{-1}$ and brown over 4 L $mg^{-1}m^{-1}$. Red shaded areas indicate times of increased discharge.*

Because DOC concentrations in stream water were insufficient for reliable NMR spectra, soil extracts were analyzed. Those extracts exhibited a broad range of $SUVA_{254}$ values (0.8 to 8.1 L $mg^{-1}m^{-1}$, Figure 8 a), with highest values measured in the base-extract sample (S2-B1). To further characterize this apparent aromatic pool structurally, solid-state ^{13}C-NMR spectra of the soil extract fractions were first evaluated for the corresponding acid-precipitated pellet fraction (P3-B1), which represents the material that was solubilized during base extraction and

subsequently precipitated during acidification (Figure 8 b). The P3-B1 spectrum showed dominant O-alkyl and carboxyl regions with minor signal contributions from the phenolic-/methoxylic, aromatic, N-alkyl/methoxyl and the anomeric groups. The acid-extractable supernatants (S1-B1, S3-B1) and the soil White Main extract (B2) exhibited a similar dominance in carboxyl, O-alkyl and aliphatic groups with some signals in the phenolic, aromatic and anomeric C regions (carbohydrate-derived C), that became especially weak in the second acid extraction step (S3-B1). Additional ^{1}H-NMR spectra are provided in SI B, Figure S7. These compositional features provide qualitative context for the functional groups potentially present in soil-derived organic material.

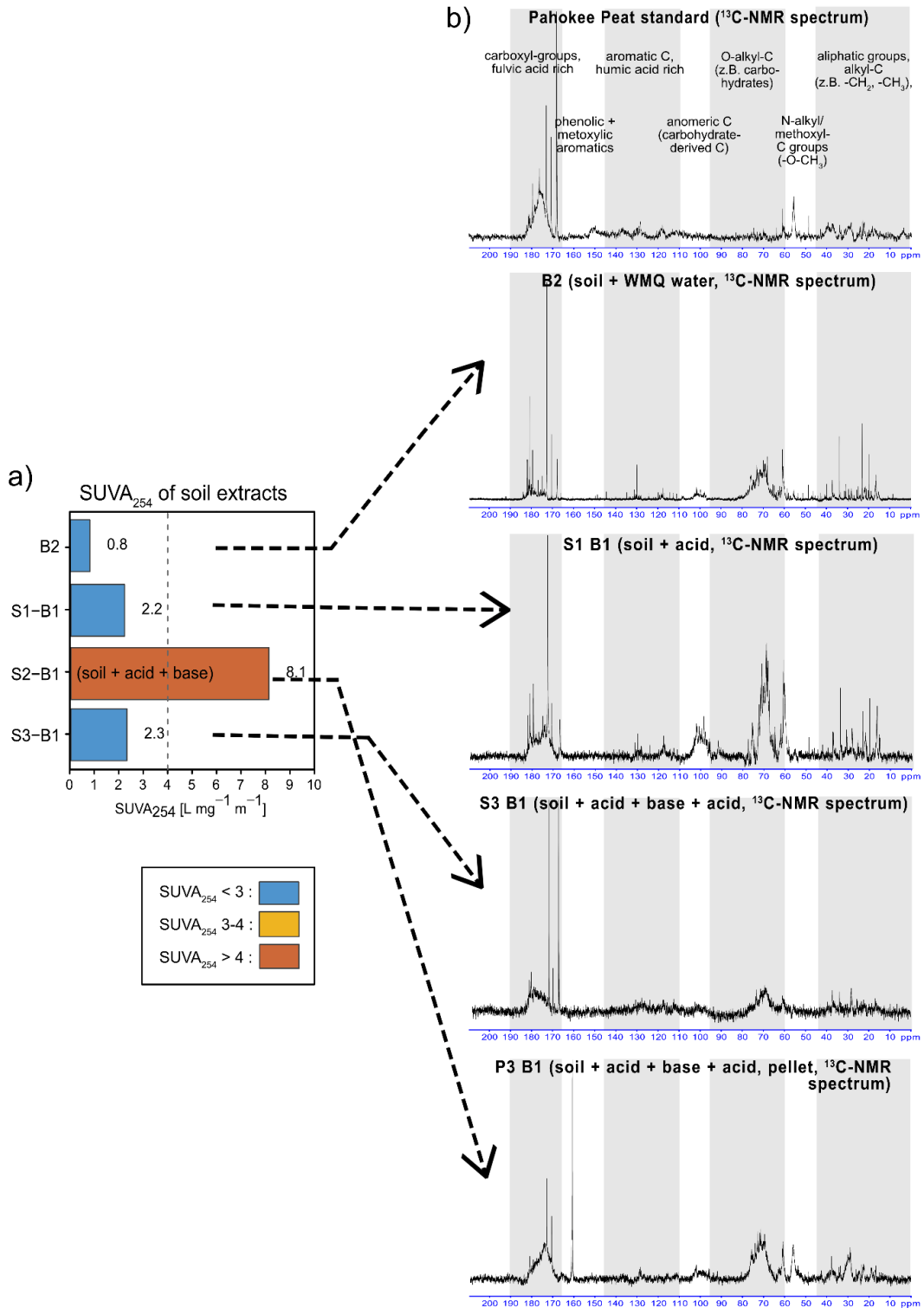

Figure 8: *a) $SUVA_{254nm}$ [L $mg^{-1}m^{-1}$] values of soil extracts (SI B, Figure S2) obtained by sequential acid-base extraction (S1-B1 -> S3-B1) or by suspension in White Main water (B2). Soil extracts were required to achieve sufficient organic carbon for ^{13}C-NMR analysis. b) ^{13}C-NMR spectra of soil extract fractions (B2, S1-B1, S3-B1, P3-B1; SI B, Figure S2) compared to the Pahokee Peat standard (PPHA). Grey- and white-shaded areas indicate the major carbon functional group ranges. Chemical shift [ppm] is plotted against relative signal intensities [-]. The P3-B1-NMR spectrum corresponds to the base-extractable fraction S2-B1 (a). P3-B1 represents the humic-acid precipitate formed during subsequent acidification, reflecting originally suspended material during base-extraction.*

4. Discussion

4.1 Baseflow dynamics: a physically dominated CO_2 system

During baseflow, the White Main operated as a physically controlled CO_2 system in which DIC speciation remained internally consistent, with no indication of dominant proton-active inputs or major solute perturbations.

Along the transect, pCO_2, F_{CO2} and c(DIC) declined downstream, while pH increased and $\delta^{13}C_{DIC}$ values became progressively enriched (Figure 2). This pattern is consistent with physically dominated CO_2 evasion and associated isotopic enrichment through preferential escape of $^{12}CO_2$ (Doctor et al., 2008; Marx et al., 2017; Polsenaere and Abril, 2012). The strongest responses occurred at hydraulically turbulent reaches (M1-M2, M7), where steep gradients enhanced gas transfer velocities (k_{600}) and promoted rapid atmospheric exchange (Guseva et al., 2021; Noss et al., 2018; Raymond et al., 2012; Zappa et al., 2007). Together with small charge-balance deviations (Figure 4 a), these observations indicate a regime dominated by physical evasion and mixing processes over chemically reactive inputs. Comparable baseflow behavior has been reported from other dilute, granitic headwaters, where limited carbonate buffering and low-ionic strength constrain alkalinity and maintain a DIC system dominated by $CO_{2(aq)}$ and HCO_3^- at pH <6 (Figure 2 c, d; Plummer and Busenberg, 1982). Under such stable discharge conditions, inputs of proton-active organic matter or reduced solutes are typically minor, reflecting limited soil-stream connectivity (Doctor et al., 2008; Grabs et al., 2012). While small contributions from heterogeneous groundwater, soil-derived acidity or colloidal phases cannot be excluded (Kaiser and Kalbitz, 2012; Pérez-Rodríguez and Biester, 2022), the overall coherence of DIC-alkalinity-pH coupling and the absence of marked solute anomalies suggest that such influences, if present, were negligible during baseflow. Within this rather stable chemical regime, thermodynamically based calculations of pCO_2 and F_{CO2} appear most reliable, as the assumptions regarding alkalinity,

pH, and DIC speciation are least likely violated (Abril et al., 2015; Raymond et al., 2012; van Geldern et al., 2015).

The spatially integrated baseflow F_{CO2} in the White Main was 3.1×10^6 mmol d^{-1} (SI B, Table S2, Figure S3), corresponding to 8.9 kg C m^{-2} during the 10 month baseflow period and 1 260 m^2. Although high-flow inputs were excluded, which are typically associated with elevated emissions (Marx et al., 2017), this value exceeds many reported full-year averages from streams and rivers between 1-5 kg C m^{-2} yr^{-1} (Cole et al., 2007; Raymond et al., 2013; Wallin et al., 2013) and falls within values observed in granite-dominated high-gradient headwaters (Horgby et al., 2019; Marx et al., 2018). These baseflow conditions therefore provide an acceptable reference against which the magnitude and nature of high-flow perturbations can be evaluated. Thus, the following sections will examine how transient discharge events introduce chemical and hydrological variability that depart from this stable baseline and may alter DIC-alkalinity-pH coupling in low-buffer granitic headwaters.

4.2 High-flow dynamics: deviations from baseflow behavior

Contrarily, high-flow conditions differed greatly from the coherent DIC-alkalinity-pH coupling observed during baseflow, with abrupt decreases in pH, alkalinity and $\delta^{13}C_{DIC}$ values, together with strongly increased charge-balance deviations at downstream sites (M5-M8, see Figure 2, 4). Simultaneously, increases in pCO_2 and F_{CO2} were restricted to periods of high discharge (Figure 2), suggesting that enhanced hydrological connectivity to surrounding soils reshaped stream chemistry over short timescales.

Similar event-driven shifts have been reported for forested stream catchments, where stormflow or snowmelt mobilize acidic, organic-rich porewaters, colloidal mineral phases and reduced solutes (Mann et al., 2014; Raymond and Saiers, 2010; Wallin et al., 2020). In contrast to well-

buffered karst systems, where discharge driven CO_2 dynamics is dampened (Liu and Han, 2021; Ran et al., 2017; Zhong et al., 2017), the granitic silicate lithology of the White Main headwater area results in very low alkalinity (<0.07 mmol L^{-1}, Figure 2 d), rendering the system highly reactive to even small hydrodynamic perturbations (Horgby et al., 2019; Marx et al., 2018).

This sensitivity is reflected by an order-of-magnitude increase in spatially integrated F_{CO2} during high flow (2.7×10^7 mmol d^{-1}), corresponding to 39.1 kg C m^{-2} during the 5-months high-flow period (SI B, Table S2, Figure S3). Together with the baseflow flux (see above), this yielded a cumulative 15-month flux of 48.0 kg C m^{-2}. Annualized to 12-months, this corresponds to a total flux of 38.0 kg C $m^{-2}yr^{-1}$, exceeding values ~35 kg C m^{-2} yr^{-1} reported for other granitic headwaters (Horgby et al., 2019; Marx et al., 2018). However, these observed flux peaks cannot be explained by physical evasion alone, as increased turbulence and k_{600} would be expected to drive declining c(DIC), together with increasing pH and $\delta^{13}C_{DIC}$ enrichments (see chapter 4.1). While our dataset does not allow identification of specific soil or groundwater endmembers, the simultaneous occurrence of hydrological peaks and chemical anomalies suggests enhanced activation of shallow, reactive soil flow paths during these events (Abesser et al., 2006; Kiewiet et al., 2020; Wallin et al., 2020). These inputs likely altered proton balance and system buffering independently of inorganic carbon (Pérez-Rodríguez and Biester, 2022), thereby disrupting standard pCO_2 and F_{CO2} calculations and supports mechanism **(i)**, whereby high flow disrupts DIC-alkalinity-pH coupling.

The following subsections explore three potential interrelated processes that may contribute to these deviations. Those are acidification and alkalinity loss, trace metal inputs and colloidal interactions, and influences of NOM, each of which has been implicated in altering DIC speciation in low-buffer headwaters but remains insufficiently characterized *in situ*.

4.2.1 Acidification and alkalinity loss during high-flow events

While gradual seasonal trends seemed not to have a direct impact, high-flow events resulted in decreases in pH, alkalinity, $\delta^{13}C_{DIC}$ and conservative ions at the downstream sites (Figure 2, 3, SI B, Figure S4). These short-lived changes coincided with pronounced increases in pCO_2 and F_{CO2} (Figure 2 a, b), yet without proportional increases in measured DIC (Figure 2 e) even though modest addition of low-alkalinity water would be expected to cause smooth shifts in DIC speciation in this weakly buffered system. This decoupling indicates that DIC speciation was primarily governed by changes in proton availability rather than by changes in inorganic carbon supply (Hunt et al., 2011; Jeanneau et al., 2015; Pérez-Rodríguez and Biester, 2022), consistent with event-driven behavior reported from other catchments (Bass et al., 2011; Liu et al., 2022; Pérez-Rodríguez and Biester, 2022; Schubert et al., 2023).

In granitic, silicate-dominated catchments, alkalinity is particularly sensitive to dilution because stormflow preferentially activates shallow soil horizons with low base-cation concentrations (Neal and Kirchner, 2000; Pérez-Rodríguez and Biester, 2022). Under such weak carbonate buffering speciation is highly sensitive to shifts in proton activity, thus even small alkalinity changes can produce disproportionately large effects on calculated pCO_2 (Plummer and Busenberg, 1982; Polsenaere and Abril, 2012). Conservative solute behavior supports this interpretation: during baseflow, slight increases in Na^+ and Cl^- downstream suggest minor contributions from additional springs and longer-residence groundwater (Figure 1 b, 3 b; Neal and Kirchner, 2000; Zhou and Cartwright, 2021; Zhou et al., 2024), while SO_4^{2-} and NO_3^- decrease likely due to mixing with reducing subsurface waters (SI B, Figure S4; Donn and Barron, 2013; Torres-Martínez et al., 2020). During high flow, this conservative background diminished as all ions significantly declined downstream, indicating possible dilution from low-ionic-strength event water from precipitation, snowmelt, and shallow soil flow (Bujak-Ozga et al., 2025; Huang et al., 2020; Jarvie et al., 1997).

Yet, dilution alone cannot explain the erratic DIC-alkalinity-pH responses. If dilution were dominant, decreasing ion concentrations would be expected to produce smooth and proportional shifts in pH, alkalinity, and $\delta^{13}C_{DIC}$, reflecting conservative mixing without additional proton sources. Instead, pH and alkalinity decreased sharply, $\delta^{13}C_{DIC}$ values shifted to more negative values, and c(DIC) decreased only minimally (Figure 2). Taken together, these patterns indicate that dilution likely acted as a detectable but non-dominant influence on water chemistry. The magnitude and direction of the observed DIC-alkalinity-pH responses cannot be explained by dilution alone and require additional proton-generating and charge-unbalancing processes, consistent with the mechanisms explored in the following sections.

4.2.2 Mobilization of redox-active species and mineral colloids during high-flow events

The mobilization of redox-sensitive elements and mineral-associated colloids, potentially from surrounding soils, is suggested by elevated concentrations of Fe, Al and Mn at the downstream sites and during high-flow events. These peaks occurred independently of major-ion patterns and were temporally aligned with periods of highest discharge. Hence, the hydrological connection between the headwater stream and the adjacent shallow, reactive horizons, which acted as sources for e.g., metal or organic inputs, appears to have been strongly reduced during baseflow.

Similar metal enrichments during stormflow have been observed in forested, acidic catchments where fluctuating water tables promote the release of Fe- and Al-bearing complexes, clay-associated particles, and other fine mineral phases (Björnerås et al., 2019; Gu et al., 2022; Pérez-Rodríguez and Biester, 2022). In turn, the presence of these constituents can affect charge balance through surface-bound protons, complexation reactions, and ligand exchange, even when present at moderate concentrations (Hunt et al., 2011; Sander et al., 2015; Tipping et al.,

2011). To evaluate whether these deviations reflected analytical artefacts or genuine compositional imbalances, CBE were calculated using major ions, trace metals and DOC concentrations (see chapter 2.3). While baseflow-CBE remained within acceptable limits (<10 %) for low-ionic-strength systems (Fritz, 1994), high-flow events resulted in strongly negative CBE values (exceeding −20%), particularly at sites M5-M8, thus indicating an apparent excess of cationic charge. Given that analytical framework, this imbalance is most plausibly explained by unaccounted-for anionic species not captured by the standard ion analysis (Figure 4 a). These anomalies coincided with only minor changes in EC (Figure 3 c) and with a clear geochemical separation between upstream and downstream sites in the PCA (Figure 4 b). This difference suggests a systematic imbalance in measured charges rather than simple dilution. Similar charge-balance deviations during hydrological flushing have been reported in other forested catchments and have been linked to episodic mobilization of unaccounted solutes (Fritz, 1994; Mosello et al., 2008).

To constrain the origin of these imbalances, redox- and pH-sensitive elements were examined together with indicators of mineral-associated transport. During baseflow, downstream increases in Fe and concurrent decreases in Mn (Figure 5 a, c), together with reductions in SO_4^{2-} and NO_3^- (SI B, Figure S4), suggested weak redox zonation and limited inputs of suboxic (low-oxygen) groundwater, consistent with observations from other headwater systems (Dwivedi et al., 2018; Wilkins et al., 2016). Lower Eh values (<500 mV, SI B, Figure S5) and PCA clustering (Figure 4 b) at downstream sites further support a distinct geochemical regime in the lower reach.

During high-flow events, these baseflow patterns were disrupted. Pronounced increases in Fe, Mn and Al at downstream sites were accompanied by small but consistent decreases in Eh and pH (Figure 2 c, SI B, Figure S5). These changes indicate occasional inflow of reduced and acidic soil waters, potentially accompanied by localized redox heterogeneity, likely originating

from riparian zones and upper soil horizons that became hydrologically connected during precipitation- and snowmelt-driven saturation-excess flow (Abesser et al., 2006; Kiewiet et al., 2020; Wang et al., 2025). Porewater measurements from soils at M4, M6, and M8, confirm acidic conditions (pH 4-5) consistent with organic acid leaching and root-mediated proton release in coniferous forest soils (Hagedorn et al., 2000). Under such conditions, Fe, Al and Mn may have been mobilized through acid-driven dissolution or partial reductive release from soil minerals (Bennett et al., 2012; Björnerås et al., 2019; Hoagland et al., 2024). Once mobilized, these metal-rich inputs likely contributed to the observed CBE deviations and local reductions in Eh and pH.

Additional contributions to the observed CBE deviations plausibly arose from the mobilization of mineral-associated colloids rather than from enhanced chemical weathering. Although saturation indices (SI) suggested thermodynamic potential for silicate dissolution during high-flow conditions (Figure 6 c), the absence of concurrent increases in Si, Na, c(DIC) or alkalinity (Figure 2 d, e, 3 b, 5 d) argues against mineral dissolution as the dominant source of the observed charge imbalance. This interpretation is further supported by short water-mineral contact times during turbulent flushing (Benettin et al., 2015; Maher, 2011), slow dissolution kinetics at pH<5 (Gudbrandsson et al., 2014), and dilution effects of meteoric and soil-derived waters, which may mask any minor weathering signals (Godsey et al., 2017).

Instead, secondary clay minerals identified at the White Main soils (illite and chlorite; Figure 6 b) likely contributed through physical mobilization as Fe- and Al- bearing colloids (Bonnet et al., 2022; Lázár et al., 2024; Zhao et al., 2023). Such minerals are known to adsorb redox-sensitive metals and can be transported as suspended aggregates during high-flow events without requiring dissolution (Aguirre et al., 2017; Baken et al., 2016; Hirst et al., 2017). ζ-potential measurements of White Main soil (M4, M6 and M8) support this interpretation: The clay-rich M8 soil exhibited significantly (p<0.05) less negative ζ-potentials than less clay-rich

samples (Figure 6 d), thus indicating reduced electrostatic repulsion and enhanced particle aggregation potential (Yan et al., 2025). Moreover, suspensions prepared in WMQ water (pH~5) showed consistently less negative ζ-potentials than those in Milli-Q water (pH~6), although this difference was not statistically significant ($p>0.05$). The consistent directional shift, nonetheless, supports the interpretation that acidification during high flow facilitated colloid mobilization (Chen et al., 2020; He et al., 2021; Lehmann et al., 2021).

In summary, high-flow events in the White Main likely promoted mobilization of metal ions and mineral-associated colloids from riparian soils through a combination of pH- and redox-driven release and physical transport. These inorganic inputs introduced additional charge carriers that modified apparent alkalinity and shifted DIC speciation towards $CO_{2(aq)}$, thereby amplifying calculated pCO_2 and F_{CO2} values through charge-unbalancing effects rather than reflecting proportional increases in in-stream CO_2 production (Polsenaere and Abril, 2012). This supports mechanism **(ii)**, which proposed that inorganic, charge-unbalancing processes contribute to DIC-alkalinity-pH decoupling during high flow. Potential interactions with organic components are addressed in the following section.

4.2.3 Organic coupling: DOC, NOM and their influence on CO_2 dynamics

While inorganic processes explained part of the high-flow deviations in pH, alkalinity and charge balance, concurrent changes in DOC quantity, composition, and metal associations point to an additional organic control on apparent proton dynamics and CO_2 behavior. During baseflow, c(DOC) remained low with $\delta^{13}C_{DOC}$ values around −28 ‰ and low stream water $SUVA_{254}$ (<3 L $mg^{-1}m^{-1}$, Figure 7), indicating dominance of aged, microbially processed C_3-derived organic matter exported via deeper subsurface pathways (Lee et al., 2023; Nkoue Ndondo et al., 2021; Schiff et al., 1990). Soil extracts and their corresponding NMR spectra further support this interpretation (Figure 8), showing fulvic-rich, weakly aromatic organic

pools (Ukalska-Jaruga et al., 2021) consistent with mineral-soil sources accessed under stable hydrological conditions (Kaiser and Kalbitz, 2012; Kindler et al., 2011; Weishaar et al., 2003), while upper organic-rich horizons were likely largely hydrologically disconnected (Doctor et al., 2008; Grabs et al., 2012). Hence, considering these stable conditions, isotope mixing indicated that DOC contributed only a minor fraction (<5%) to CO_2 evasion (see SI B, Figure S8, Table S3, SI A, S15).

High-flow events fundamentally altered this regime. The proposed reconnection to near-surface soil horizons, where microbially transformed organic matter often accumulates during baseflow (Aubert et al., 2013), led to pronounced downstream increases in DOC, elevated water and soil $SUVA_{254}$ values (>4 L mg^{-1} m^{-1}; Figure 7 a, c; 8 a), visible brownification (SI B, Figure S6; Haaland et al., 2024; Kritzberg and Ekström, 2012), concurrent Fe- and Al-peaks, and slightly enriched $\delta^{13}C_{DOC}$ values (~–26‰, Figure 5 a, b; 7 b). Together, these results suggest mobilization of more aromatic, mineral- and metal-associated organic matter from shallow soils rather than increased contributions from dissolved humic acids, which are expected to be poorly soluble in the stream's acidic pH of 4-5 during high flow (Blaurock et al., 2021; Prijac et al., 2023; Swift, 1996; Tiwari et al., 2022). Soil extractions also identified strongly aromatic NOM reservoirs that are unlikely to dissolve directly, indicating that the high-flow signal primarily reflects physical flushing of fulvic-like components and Fe-/Al-bound organic colloids destabilized during soil-stream reconnection (Anderson et al., 2021; Baglieri et al., 2014; Haaland et al., 2024; Kritzberg and Ekström, 2012; Riise et al., 2023).

Additional support for the proposed mechanism comes from isotopic mixing models, which indicate that oxidation of mobilized organic matter contributed measurably, though not predominantly, to CO_2 production during high flow. Here, DOC-derived CO_2 fractions increase to ~17-19% at downstream sites, culminating at up to ~41% at M8 (SI B, Figure S8, Table S3, SI A, S15). While indeed these values are subject to uncertainty, they are consistent with

observations from other forested headwaters where episodic NOM export enhances CO_2 evasion without fundamentally altering the dominant inorganic C pool (Gu et al., 2022; Lapierre et al., 2013). Importantly, while DOC-derived CO_2 production clearly contributed to elevated pCO_2 and F_{CO2} during high flow, it cannot fully account for the magnitude of the observed flux peaks, even when rapid CO_2 evasion and incomplete capture in measured DIC are considered.

Beyond acting as C source, mobilized NOM likely biased DIC-alkalinity-pH dynamics through its proton-active functional groups and metal-binding ligands (Bai et al., 2020; Kappler et al., 2004; Sander et al., 2015; Stern et al., 2018). Deprotonation, ligand exchange, and complexation reactions can release protons and consume alkalinity independently of DIC, while smaller contributions of non-carbonate alkalinity are insufficient to offset the net acidifying effect (Hunt et al., 2011; Tipping et al., 2011). As a result, NOM-driven proton fluxes likely have shifted DIC speciation towards $CO_{2(aq)}$, thus inflating thermodynamically based pCO_2 and F_{CO2} results during high-flow events without requiring enhanced in-stream CO_2 production (Abril et al., 2015; Hunt et al., 2011; Jeanneau et al., 2015). Hence, these findings support mechanism **(iii)**, suggesting that event-driven mobilization of organic- and metal-rich soil materials can exert a disproportionate control on DIC-system behavior in weakly buffered granitic headwater streams.

5. Conclusions

This study investigated DIC-system dynamics in a granitic, forested headwater stream (White Main) characterized by low alkalinity and event-driven hydrological connectivity to surrounding soils. Such systems are inherently sensitive to short-term chemical disruptions yet are commonly assessed by using standard thermodynamically based approaches to determine pCO_2 and CO_2 fluxes.

Under baseflow conditions, the White Main exhibited spatially coherent and temporally stable DIC-alkalinity-pH coupling, with downstream decreases in pCO_2, F_{CO2}, and enrichment in $\delta^{13}C_{DIC}$ consistent with physically dominated CO_2 evasion. Low and stable alkalinity, small charge-balance deviations, and weak variability in DOC and redox-sensitive elements indicate that, during these periods, pCO_2 and F_{CO2} calculations provide a reasonable approximation of in-stream CO_2 conditions.

In contrast, high-flow events produced pronounced but short-lived deviations from this baseflow state. Decreases in pH, alkalinity and $\delta^{13}C_{DIC}$, together with increasing charge-balance deviations, elevated concentrations of Fe, Al, and Mn, as well as shifts in DOC quantity and composition, collectively indicate enhanced connectivity to shallow, reactive soil horizons. These inputs introduced inorganic and organic charge carriers capable of altering proton balances independently of inorganic C, thereby temporally disrupting DIC-alkalinity-pH assumptions. As a result, reconstructed pCO_2 and CO_2 fluxes increased during high flow without corresponding increases in measured DIC, indicating that rapid CO_2 evasion likely masked concurrent in-stream CO_2 production and that the observed flux peaks partly reflect methodological artefacts rather than solely enhanced CO_2 generation.

Taken together, these results demonstrate that event-driven mobilization of soil-derived solutes, mineral-associated colloids, and natural organic matter can transiently bias thermodynamically-based pCO_2 and F_{CO2} calculations, thereby reducing the reliability of these indirect approaches

in weakly buffered headwater streams, as they may systematically overestimate CO_2 fluxes by misattributing chemically induced shifts in alkalinity and proton balance to increased CO_2 production. While event-driven DOC inputs indicate transient activation of soil-derived carbon sources, the observed flux peaks arise primarily from short-term chemical disruptions that violate the assumptions underlying commonly applied DIC-equilibrium calculations, rather than from sustained changes in C sources or proportional increases in in-stream CO_2 production. While the relative contributions of individual mechanisms cannot be fully resolved with the available data, this limitation reflects the inherently interlinked nature of these underlying processes. Instead, the interplay of multiple independent indicators supports a conceptual model in which hydrological pulses interacting with biogeochemical controls, rather than seasonality or discharge magnitude alone, dominate DIC speciation and CO_2 loss.

This study highlights the need for caution when interpreting thermodynamically based CO_2 fluxes, particularly in low-alkalinity headwaters and especially during periods of enhanced soil-stream connectivity. More broadly, it suggests that granitic headwater streams function as sensitive indicators of hydrologically driven chemical disturbances, making them valuable natural laboratories for investigating transient controls on inland-water C cycling under current and future climate conditions.

Funding details

This work was supported by the German Research Foundation (DFG) under Grant numbers GE 2338/4-1 and BA 2207/27-1.

Acknowledgements

We thank the *Bayerische Staatsforsten AöR – Forstbetrieb Fichtelberg* for granting access to the forest roads of the Ochsenkopf area. We are especially grateful to Lukas Bachmeier, Julia

Schmitz, Jan Maier, Aixala Gaillard and Sachintha Senarathne for their committed and enthusiastic support during fieldwork.

Our heartfelt thanks also go to Christian Hanke, Irene Wein, Anja Schuster and Mark Bauer for their reliable technical and analytical support during laboratory work. We gratefully acknowledge Dr. Stefan Krumm for conducting the XRD soil measurement, and Leila Pourtalebijahromi and Maja Dörfner for sharing their expertise and measurement equipment during the ζ-potential analyses.

We further thank Prof. Dr. Stefan B. Haderlein (University of Tübingen) for generously providing the Pahokee Peat Standard used in the NMR analyses.

Additional thanks go to Dr. Ute Schmidt and the Soilsciences Laboratory (FAU Erlangen, Institute of Geographie) for soil size measurements.

We are also very grateful to Prof. Dr. Kathrin Castiglione and Patrik Blenk from the Chair of Bioprocess Engineering (BVT) Erlangen for kindly providing laboratory equipment and resources for the NMR extraction, as well as UV-VIS and fluorescence analyses.

Finally, the authors acknowledge the use of ChatGPT-4 (OpenAI) for language editing and minor code formatting; all analyses were verified by the authors.

Disclosure statement

The authors report there are no competing interests to declare.

Author contributions:

- Christina Schubert: Conceptualization, Data curation, Formal analysis, Investigation, Methodology, Visualization, Writing – original draft

- Robert van Geldern: Funding acquisition, Project administration, Resources, Supervision, Validation, Writing – review and editing
- Marcus Speck: Data curation, Resources, Writing – review and editing
- Christian Placht: Data curation, Resources, Writing – review and editing, Writing – original draft
- Harald Maid: Data curation, Resources, Methodology, Writing – review and editing, Writing – original draft
- Johannes Barth: Funding acquisition, Validation, Resources, Writing – review and editing
- Anna-Neva Visser: Conceptualization, Data curation, Methodology, Formal analysis, Resources, Project administration, Investigation, Supervision, Validation, Writing – review and editing

Supporting online information

Supporting information A with supporting analytical procedures and Supporting information B with additional Figures and Tables.

6. References

Abesser, C., Robinson, R., Soulsby, C., 2006. Iron and manganese cycling in the storm runoff of a Scottish upland catchment. Journal of Hydrology, 326(1): 59-78. DOI:10.1016/j.jhydrol.2005.10.034

Abril, G., Bouillon, S., Darchambeau, F., Teodoru, C.R., Marwick, T.R., Tamooh, F., Ochieng Omengo, F., Geeraert, N., Deirmendjian, L., Polsenaere, P., Borges, A.V., 2015. Technical Note: Large overestimation of pCO_2 calculated from pH and alkalinity in acidic, organic-rich freshwaters. Biogeosciences, 12(1): 67-78. DOI:10.5194/bg-12-67-2015

Adler, T., Underwood, K.L., Rizzo, D.M., Harpold, A., Sterle, G., Li, L., Wen, H., Stinson, L., Bristol, C., Stewart, B., Lini, A., Perdrial, N., Perdrial, J.N., 2021. Drivers of Dissolved Organic Carbon Mobilization From Forested Headwater Catchments: A Multi Scaled Approach. Frontiers in Water, 3. DOI:10.3389/frwa.2021.578608

Aguirre, A.A., Derry, L.A., Mills, T.J., Anderson, S.P., 2017. Colloidal transport in the Gordon Gulch catchment of the Boulder Creek CZO and its effect on C-Q relationships for silicon. Water Resources Research, 53(3): 2368-2383. DOI:10.1002/2016WR019730

Anderson, L.E., Trueman, B.F., Dunnington, D.W., Gagnon, G.A., 2021. Relative importance of organic- and iron-based colloids in six Nova Scotian lakes. npj Clean Water, 4(1): 26. DOI:10.1038/s41545-021-00115-4

Appelo, C.A.J., Postma, D., 2004. Geochemistry, Groundwater and Pollution (2nd ed.). CRC Press, London. DOI:10.1201/9781439833544

Attermeyer, K., Catalán, N., Einarsdottir, K., Freixa, A., Groeneveld, M., Hawkes, J.A., Bergquist, J., Tranvik, L.J., 2018. Organic Carbon Processing During Transport Through Boreal Inland Waters: Particles as Important Sites. Journal of Geophysical Research: Biogeosciences, 123(8): 2412-2428. DOI:10.1029/2018JG004500

Aubert, A.H., Gascuel-Odoux, C., Gruau, G., Akkal, N., Faucheux, M., Fauvel, Y., Grimaldi, C., Hamon, Y., Jaffrézic, A., Lecoz-Boutnik, M., Molénat, J., Petitjean, P., Ruiz, L., Merot, P., 2013. Solute transport dynamics in small, shallow groundwater-dominated agricultural catchments: insights from a high-frequency, multisolute 10 yr-long monitoring study. Hydrology and Earth System Sciences, 17(4): 1379-1391. DOI:10.5194/hess-17-1379-2013

Aufdenkampe, A.K., Mayorga, E., Raymond, P.A., Melack, J.M., Doney, S.C., Alin, S.R., Aalto, R.E., Yoo, K., 2011. Riverine coupling of biogeochemical cycles between land, oceans, and atmosphere. Frontiers in Ecology and the Environment, 9(1): 53-60. DOI:10.1890/100014

Baglieri, A., Vindrola, D., Gennari, M., Negre, M., 2014. Chemical and spectroscopic characterization of insoluble and soluble humic acid fractions at different pH values. Chemical and Biological Technologies in Agriculture, 1(1): 9. DOI:10.1186/s40538-014-0009-x

Bai, Y., Subdiaga, E., Haderlein, S.B., Knicker, H., Kappler, A., 2020. High-pH and anoxic conditions during soil organic matter extraction increases its electron-exchange capacity and ability to stimulate microbial Fe (III) reduction by electron shuttling. Biogeosciences, 17(3): 683-698. DOI:10.5194/bg-17-683-2020

Baken, S., Regelink, I.C., Comans, R.N.J., Smolders, E., Koopmans, G.F., 2016. Iron-rich colloids as carriers of phosphorus in streams: A field-flow fractionation study. Water Research, 99: 83-90. DOI:10.1016/j.watres.2016.04.060

Bass, A.M., Bird, M.I., Liddell, M.J., Nelson, P.N., 2011. Fluvial dynamics of dissolved and particulate organic carbon during periodic discharge events in a steep tropical rainforest catchment. Limnology and Oceanography, 56(6): 2282-2292. DOI:10.4319/lo.2011.56.6.2282

Battin, T.J., Luyssaert, S., Kaplan, L.A., Aufdenkampe, A.K., Richter, A., Tranvik, L.J., 2009. The boundless carbon cycle. Nature Geoscience, 2(9): 598-600. DOI:10.1038/ngeo618

Bayerisches Landesamt für Umwelt, 2024. UmweltAtlas Geologie, Accessible at: https://www.umweltatlas.bayern.de/mapapps/resources/apps/umweltatlas [Accessed on 15th of October 2024].

Bayerisches Landesamt für Umwelt, 2025. Gewässerkundlicher Dienst Bayern, Accessible at: https://www.gkd.bayern.de/ [Accessed on 7th of July 2025].

Benettin, P., Bailey, S.W., Campbell, J.L., Green, M.B., Rinaldo, A., Likens, G.E., McGuire, K.J., Botter, G., 2015. Linking water age and solute dynamics in streamflow at the Hubbard Brook Experimental Forest, NH, USA. Water Resources Research, 51(11): 9256-9272. DOI:10.1002/2015WR017552

Bennett, W.W., Teasdale, P.R., Panther, J.G., Welsh, D.T., Zhao, H., Jolley, D.F., 2012. Investigating Arsenic Speciation and Mobilization in Sediments with DGT and DET: A Mesocosm Evaluation of Oxic-Anoxic Transitions. Environmental Science & Technology, 46(7): 3981-3989. DOI:10.1021/es204484k

Björnerås, C., Škerlep, M., Floudas, D., Persson, P., Kritzberg, E.S., 2019. High sulfate concentration enhances iron mobilization from organic soil to water. Biogeochemistry, 144(3): 245-259. DOI:10.1007/s10533-019-00581-6

Blaurock, K., Beudert, B., Gilfedder, B.S., Fleckenstein, J.H., Peiffer, S., Hopp, L., 2021. Low hydrological connectivity after summer drought inhibits DOC export in a forested headwater catchment. Hydrology and Earth System Sciences, 25(9): 5133-5151. DOI:10.5194/hess-25-5133-2021

Bonnet, M., Caner, L., Siitari-Kauppi, M., Mazurier, A., Mexias, A.S., Dani, N., Sardini, P., 2022. Weathering of Viamão granodiorite, South Brazil: Part 1 – Clay minerals formation and increase in total porosity. Geoderma, 424: 115968. DOI:10.1016/j.geoderma.2022.115968

Bujak-Ozga, I., von Freyberg, J., Zimmer, M., Rinaldo, A., Benettin, P., van Meerveld, I., 2025. Changes in the flowing drainage network and stream chemistry during rainfall events for two pre-Alpine catchments. Hydrology and Earth System Sciences, 29(11): 2339-2359. DOI:10.5194/hess-29-2339-2025

Burger, D.J., Vogel, J., Kooijman, A.M., Bol, R., de Rijke, E., Schoorl, J., Lücke, A., Gottselig, N., 2021. Colloidal catchment response to snowmelt and precipitation events differs in a forested headwater catchment. Vadose Zone Journal, 20(3): e20126. DOI:10.1002/vzj2.20126

Carter, A.M., DelVecchia, A.G., Bernhardt, E.S., 2022. Patterns and Drivers of Dissolved Gas Concentrations and Fluxes Along a Low Gradient Stream. Journal of Geophysical Research: Biogeosciences, 127(11): e2022JG007048. DOI:10.1029/2022JG007048

Chan, C.N., Tsang, C.L., Lee, F., Liu, B., Ran, L., 2021. Rapid Loss of Dissolved CO_2 From a Subtropical Steep Headwater Stream. Frontiers in Earth Science, 9: 741678. DOI:10.3389/feart.2021.741678

Chen, Y., Ma, J., Wu, X., Weng, L., Li, Y., 2020. Sedimentation and Transport of Different Soil Colloids: Effects of Goethite and Humic Acid, Water. DOI:10.3390/w12040980

Cincotta, M.M., Perdrial, J.N., Shavitz, A., Libenson, A., Landsman-Gerjoi, M., Perdrial, N., Armfield, J., Adler, T., Shanley, J.B., 2019. Soil Aggregates as a Source of Dissolved Organic Carbon to Streams: An Experimental Study on the Effect of Solution Chemistry on Water Extractable Carbon. Frontiers in Environmental Science, 7: 172. DOI:10.3389/fenvs.2019.00172

Clow, D.W., Striegl, R.G., Dornblaser, M.M., 2021. Spatiotemporal Dynamics of CO_2 Gas Exchange From Headwater Mountain Streams. Journal of Geophysical Research: Biogeosciences, 126(9): e2021JG006509. DOI:10.1029/2021JG006509

Cole, J.J., Prairie, Y.T., Caraco, N.F., McDowell, W.H., Tranvik, L.J., Striegl, R.G., Duarte, C.M., Kortelainen, P., Downing, J.A., Middelburg, J.J., Melack, J., 2007. Plumbing the Global Carbon Cycle: Integrating Inland Waters into the Terrestrial Carbon Budget. Ecosystems, 10(1): 172-185. DOI:10.1007/s10021-006-9013-8

Dawson, J.J.C., Bakewell, C., Billett, M.F., 2001. Is in-stream processing an important control on spatial changes in carbon fluxes in headwater catchments? Science of The Total Environment, 265(1): 153-167. DOI:10.1016/S0048-9697(00)00656-2

Demers, J.D., Driscoll, C.T., Shanley, J.B., 2010. Mercury mobilization and episodic stream acidification during snowmelt: Role of hydrologic flow paths, source areas, and supply of dissolved organic carbon. Water Resources Research, 46(1). DOI:10.1029/2008WR007021

Dickson, A.G., Sabine, C.L., Christian, J.R., 2007. Guide to best practices for ocean CO_2 measurements. PICES Special Publication, 191 pp. Accessible at: http://www.cdiac.ornl.gov/oceans/Handbook_2007.html [Accessed on 30th of October 2025].

Doctor, D.H., Kendall, C., Sebestyen, S.D., Shanley, J.B., Ohte, N., Boyer, E.W., 2008. Carbon isotope fractionation of dissolved inorganic carbon (DIC) due to outgassing of carbon dioxide from a headwater stream. Hydrological Processes, 22(14): 2410-2423. DOI:10.1002/hyp.6833

Doebelin, N., Kleeberg, R., 2015. Profex: A graphical user interface for the Rietveld refinement program BGMN. Journal of Applied Crystallography, 48: 1573-1580. DOI:10.1107/S1600576715014685

Donn, M.J., Barron, O.V., 2013. Biogeochemical processes in the groundwater discharge zone of urban streams. Biogeochemistry, 115(1): 267-286. DOI:10.1007/s10533-013-9833-5

Duvert, C., Butman, D.E., Marx, A., Ribolzi, O., Hutley, L.B., 2018. CO_2 evasion along streams driven by groundwater inputs and geomorphic controls. Nature Geoscience, 11(11): 813-818. DOI:10.1038/s41561-018-0245-y

DWD Climate Data Center (CDC), 2025. Tägliche Stationsmessungen Niederschlagshöhe in mm für Deutschland, Version v21.3. Accessible at: https://cdc.dwd.de/portal/202209231028/mapview [Accessed on 7th of July 2025].

Dwivedi, D., Steefel, C.I., Arora, B., Newcomer, M., Moulton, J.D., Dafflon, B., Faybishenko, B., Fox, P., Nico, P., Spycher, N., Carroll, R., Williams, K.H., 2018. Geochemical Exports to River From the Intrameander Hyporheic Zone Under Transient Hydrologic Conditions: East River Mountainous Watershed, Colorado. Water Resources Research, 54(10): 8456-8477. DOI:10.1029/2018WR023377

Fisher, R.A., 1992. Statistical Methods for Research Workers. In: Kotz, S., Johnson, N.L. (Eds.), Breakthroughs in Statistics: Methodology and Distribution. Springer New York, New York, NY, pp. 66-70. DOI:10.1007/978-1-4612-4380-9_6

Fritz, S.J., 1994. A Survey of Charge-Balance Errors on Published Analyses of Potable Ground and Surface Waters. Groundwater, 32(4): 539-546. DOI:10.1111/j.1745-6584.1994.tb00888.x

Godsey, S., Hartmann, J., Kirchner, J., 2017. Catchment chemostasis revisited: Water quality responds differently to variations in weather and climate. Hydrological Processes, 33: 3056-3069. DOI:10.1002/hyp.13554

Grabs, T., Bishop, K., Laudon, H., Lyon, S.W., Seibert, J., 2012. Riparian zone hydrology and soil water total organic carbon (TOC): implications for spatial variability and upscaling of lateral riparian TOC exports. Biogeosciences, 9(10): 3901-3916. DOI:10.5194/bg-9-3901-2012

Gu, S., Xu, Y.J., Li, S., 2022. Unravelling the spatiotemporal variation of pCO_2 in low order streams: Linkages to land use and stream order. Science of The Total Environment, 820: 153226. DOI:10.1016/j.scitotenv.2022.153226

Gudbrandsson, S., Wolff-Boenisch, D., Gislason, S.R., Oelkers, E.H., 2014. Experimental determination of plagioclase dissolution rates as a function of its composition and pH at 22°C. Geochimica et Cosmochimica Acta, 139: 154-172. DOI:10.1016/j.gca.2014.04.028

Guseva, S., Aurela, M., Cortés, A., Kivi, R., Lotsari, E., MacIntyre, S., Mammarella, I., Ojala, A., Stepanenko, V., Uotila, P., Vähä, A., Vesala, T., Wallin, M.B., Lorke, A., 2021. Variable Physical Drivers of Near-Surface Turbulence in a Regulated River. Water Resources Research, 57(11): e2020WR027939. DOI:10.1029/2020WR027939

Haaland, S., Hejzlar, J., Eikebrokk, B., Orderud, G., Paule-Mercado, M.C., Porcal, P., Sláma, J., Vogt, R.D., 2024. Predicting the dissolved natural organic matter (DNOM) concentration and the specific ultraviolet absorption (sUVa) index in a browning central European stream. Ecological Indicators, 165: 112200. DOI:10.1016/j.ecolind.2024.112200

Hagedorn, F., Schleppi, P., Waldner, P., Flühler, H., 2000. Export of dissolved organic carbon and nitrogen from Gleysol dominated catchments – the significance of water flow paths. Biogeochemistry, 50(2): 137-161. DOI:10.1023/A:1006398105953

He, Y., Yang, M., Huang, R., Wang, Y., Ali, W., 2021. Soil organic matter and clay zeta potential influence aggregation of a clayey red soil (Ultisol) under long-term fertilization. Scientific Reports, 11(1): 20498. DOI:10.1038/s41598-021-99769-w

Herrmann, M., Najjar, R.G., Da, F., Friedman, J.R., Friedrichs, M.A.M., Goldberger, S., Menendez, A., Shadwick, E.H., Stets, E.G., St-Laurent, P., 2020. Challenges in Quantifying Air-Water Carbon Dioxide Flux Using Estuarine Water Quality Data: Case Study for Chesapeake Bay. Journal of Geophysical Research: Oceans, 125(7): e2019JC015610. DOI:10.1029/2019JC015610

Hirst, C., Andersson, P.S., Shaw, S., Burke, I.T., Kutscher, L., Murphy, M.J., Maximov, T., Pokrovsky, O.S., Mörth, C.-M., Porcelli, D., 2017. Characterisation of Fe-bearing particles and colloids in the Lena River basin, NE Russia. Geochimica et Cosmochimica Acta, 213: 553-573. DOI:10.1016/j.gca.2017.07.012

Hoagland, B., Rasmussen Kalen, L., Singha, K., Spear John, R., Navarre-Sitchler, A., 2024. Metal-oxide precipitation influences microbiome structure in hyporheic zones receiving acid rock drainage. Applied and Environmental Microbiology, 90(3): e01987-23. DOI:10.1128/aem.01987-23

Hope, D., Dawson, J.J.C., Cresser, M.S., Billett, M.F., 1995. A method for measuring free CO_2 in upland streamwater using headspace analysis. Journal of Hydrology, 166(1): 1-14. DOI:10.1016/0022-1694(94)02628-O

Horgby, Å., Segatto, P.L., Bertuzzo, E., Lauerwald, R., Lehner, B., Ulseth, A.J., Vennemann, T.W., Battin, T.J., 2019. Unexpected large evasion fluxes of carbon dioxide from turbulent streams draining the world's mountains. Nature Communications, 10(1): 4888. DOI:10.1038/s41467-019-12905-z

Huang, G.-Z., Hsu, T.-C., Yu, C.-K., Huang, J.-C., Lin, T.-C., 2020. Dilution and precipitation dominated regulation of stream water chemistry of a volcanic watershed. Journal of Hydrology, 583: 124564. DOI:10.1016/j.jhydrol.2020.124564

Hunt, C.W., Salisbury, J.E., Vandemark, D., 2011. Contribution of non-carbonate anions to total alkalinity and overestimation of pCO_2 in New England and New Brunswick rivers. Biogeosciences, 8(10): 3069-3076. DOI:10.5194/bg-8-3069-2011

Hunter, R.J., 1981. Zeta Potential in Colloid Science: Principles and Applications. Academic Press, London. DOI:10.1016/C2013-0-07389-6

International Humic Substances Society, 2024. Isolation of IHSS Soil Fulvic and Humic Acids. Accessible at: https://humic-substances.org/ [Accessed on 14th of July 2025].

Jarvie, H.P., Neal, C., Leach, D.V., Ryland, G.P., House, W.A., Robson, A.J., 1997. Major ion concentrations and the inorganic carbon chemistry of the Humber rivers. Science of The Total Environment, 194-195: 285-302. DOI:10.1016/S0048-9697(96)05371-5

Jeanneau, L., Denis, M., Pierson-Wickmann, A.C., Gruau, G., Lambert, T., Petitjean, P., 2015. Sources of dissolved organic matter during storm and inter-storm conditions in a lowland headwater catchment: constraints from high-frequency molecular data. Biogeosciences, 12(14): 4333-4343. DOI:10.5194/bg-12-4333-2015

Johnson, M.S., Lehmann, J., Riha, S.J., Krusche, A.V., Richey, J.E., Ometto, J.P.H.B., Couto, E.G., 2008. CO_2 efflux from Amazonian headwater streams represents a significant fate for deep soil respiration. Geophysical Research Letters, 35(17): L17401. DOI:10.1029/2008GL034619

Kaiser, K., 2003. Sorption of natural organic matter fractions to goethite (α-FeOOH): effect of chemical composition as revealed by liquid-state ^{13}C NMR and wet-chemical analysis. Organic Geochemistry, 34(11): 1569-1579. DOI:10.1016/S0146-6380(03)00120-7

Kaiser, K., Kalbitz, K., 2012. Cycling downwards – dissolved organic matter in soils. Soil Biology and Biochemistry, 52: 29-32. DOI:10.1016/j.soilbio.2012.04.002

Kappler, A., Benz, M., Schink, B., Brune, A., 2004. Electron shuttling via humic acids in microbial iron(III) reduction in a freshwater sediment. FEMS Microbiology Ecology, 47(1): 85-92. DOI:10.1016/S0168-6496(03)00245-9

Kiewiet, L., van Meerveld, I., Stähli, M., Seibert, J., 2020. Do stream water solute concentrations reflect when connectivity occurs in a small, pre-Alpine headwater catchment? Hydrology and Earth System Sciences, 24(7): 3381-3398. DOI:10.5194/hess-24-3381-2020

Kindler, R., Siemens, J.A.N., Kaiser, K., Walmsley, D.C., Bernhofer, C., Buchmann, N., Cellier, P., Eugster, W., Gleixner, G., Grünwald, T., Heim, A., Ibrom, A., Jones, S.K., Jones, M., Klumpp, K., Kutsch, W., Larsen, K.S., Lehuger, S., Loubet, B., McKenzie, R., Moors, E., Osborne, B., Pilegaard, K.I.M., Rebmann, C., Saunders, M., Schmidt, M.W.I., Schrumpf, M., Seyfferth, J., Skiba, U.T.E., Soussana, J.-F., Sutton, M.A., Tefs, C., Vowinckel, B., Zeeman, M.J., Kaupenjohann, M., 2011. Dissolved carbon leaching from soil is a crucial component of the net ecosystem carbon balance. Global Change Biology, 17(2): 1167-1185. DOI:10.1111/j.1365-2486.2010.02282.x

Knutson, J., Clayer, F., Norling, M., Lepistö, A., Marttila, H., Futter, M.N., Eklöf, K., de Wit, H., 2021. Hydrological controls of DOC export from Nordic headwater catchments, EGU General Assembly 2021, online, https://doi.org/10.5194/egusphere-egu21-15119.

Kokic, J., Sahlée, E., Sobek, S., Vachon, D., Wallin, M.B., 2018. High spatial variability of gas transfer velocity in streams revealed by turbulence measurements. Inland Waters, 8(4): 461-473. DOI:10.1080/20442041.2018.1500228

Kritzberg, E.S., Ekström, S.M., 2012. Increasing iron concentrations in surface waters - a factor behind brownification? Biogeosciences, 9(4): 1465-1478. DOI:10.5194/bg-9-1465-2012

Krivdin, Leonid B., 2024. Liquid-Phase NMR of Humic and Fulvic Acids. Magnetic Resonance in Chemistry, 63(2): 128-150. DOI:10.1002/mrc.5493

Lapierre, J.-F., Guillemette, F., Berggren, M., del Giorgio, P.A., 2013. Increases in terrestrially derived carbon stimulate organic carbon processing and CO_2 emissions in boreal aquatic ecosystems. Nature Communications, 4(1): 2972. DOI:10.1038/ncomms3972

Lauerwald, R., Allen, G.H., Deemer, B.R., Liu, S., Maavara, T., Raymond, P., Alcott, L., Bastviken, D., Hastie, A., Holgerson, M.A., Johnson, M.S., Lehner, B., Lin, P., Marzadri, A., Ran, L., Tian, H., Yang, X., Yao, Y., Regnier, P., 2023. Inland Water Greenhouse Gas Budgets for RECCAP2: 2. Regionalization and Homogenization of Estimates. Global Biogeochemical Cycles, 37(5): e2022GB007658. DOI:10.1029/2022GB007658

Lázár, K., Máthé, Z., Németh, T., Kovács-Kis, V., Stichleutner, S., Kovács, I., 2024. Iron-Bearing Minerals in the Boda Claystone Formation: Correspondences with Stages of Evolution Revealed by Mössbauer Spectroscopy, Minerals. DOI:10.3390/min14020196

Lee, E.-J., Shin, Y., Lee, K., Lee, S.-C., Cha, J.-Y., Oh, N.-H., 2023. Comparison of organic carbon properties in extracted soil solutions obtained underneath Cryptomeria japonica and Quercus acutissima and its implication on stream dissolved organic carbon. Forest Science and Technology, 19(4): 296-308. DOI:10.1080/21580103.2023.2265966

Lehmann, K., Lehmann, R., Totsche, K.U., 2021. Event-driven dynamics of the total mobile inventory in undisturbed soil account for significant fluxes of particulate organic carbon. Science of The Total Environment, 756: 143774. DOI:10.1016/j.scitotenv.2020.143774

Levchuk, I., Rueda Márquez, J.J., Sillanpää, M., 2018. Removal of natural organic matter (NOM) from water by ion exchange – A review. Chemosphere, 192: 90-104. DOI:10.1016/j.chemosphere.2017.10.101

Levene, H., 1960. Robust tests for equality of variances. In: Olkin, I. (Ed.), Contributions to Probability and Statistics: Essays in Honor of Harold Hotelling Stanford studies in mathematics and statistics. Stanford University Press, pp. 278-292.

Liu, J., Han, G., 2021. Controlling factors of riverine CO_2 partial pressure and CO_2 outgassing in a large karst river under base flow condition. Journal of Hydrology, 593: 125638. DOI:10.1016/j.jhydrol.2020.125638

Liu, X., Lu, X., Yu, R., Sun, H., Li, Y., Qi, Z., Xue, H., Zhang, Z., Cao, Z., Liu, T., Lu, C., 2022. Sediment and carbon dynamics during an episodic flood in an intermittent river. Ecosphere, 13(10): e4248. DOI:10.1002/ecs2.4248

Maher, K., 2011. The role of fluid residence time and topographic scales in determining chemical fluxes from landscapes. Earth and Planetary Science Letters, 312(1): 48-58. DOI:10.1016/j.epsl.2011.09.040

Mann, P.J., Spencer, R.G.M., Dinga, B.J., Poulsen, J.R., Hernes, P.J., Fiske, G., Salter, M.E., Wang, Z.A., Hoering, K.A., Six, J., Holmes, R.M., 2014. The biogeochemistry of carbon across a gradient of streams and rivers within the Congo Basin. Journal of Geophysical Research: Biogeosciences, 119(4): 687-702. DOI:10.1002/2013JG002442

Marx, A., Conrad, M., Aizinger, V., Prechtel, A., van Geldern, R., Barth, J.A.C., 2018. Groundwater data improve modelling of headwater stream CO_2 outgassing with a stable DIC isotope approach. Biogeosciences, 15(10): 3093-3106. DOI:10.5194/bg-15-3093-2018

Marx, A., Dusek, J., Jankovec, J., Sanda, M., Vogel, T., van Geldern, R., Hartmann, J., Barth, J.A.C., 2017. A review of CO_2 and associated carbon dynamics in headwater streams: A global perspective. Reviews of Geophysics, 55(2): 560-585. DOI:10.1002/2016RG000547

McCallister, S.L., Ishikawa, N.F., Kothawala, D.N., 2018. Biogeochemical tools for characterizing organic carbon in inland aquatic ecosystems. Limnology and Oceanography Letters, 3(6): 444-457. DOI:10.1002/lol2.10097

Mosello, R., Amoriello, T., Benham, S., Clarke, N., Derome, J., Derome, K., Genouw, G., Koenig, N., Orrù, A., Tartari, G., Thimonier, A., Ulrich, E., Lindroos, A.J., 2008. Validation of chemical analyses of atmospheric deposition on forested sites in Europe: 2. DOC concentration as an estimator of the organic ion charge. Journal of Limnology, 67(1): 1-14. DOI:10.4081/jlimnol.2008.1

Nayna, O.K., Begum, M.S., Ran, L., Park, J.-H., 2021. Improving Carbonate Equilibria-Based Estimation of pCO_2 in Anthropogenically Impacted River Systems. Frontiers in Earth Science, 9: 778215. DOI:10.3389/feart.2021.778215

Neal, C., Kirchner, J.W., 2000. Sodium and chloride levels in rainfall, mist, streamwater and groundwater at the Plynlimon catchments, mid-Wales: inferences on hydrological and chemical controls. Hydrology and Earth System Sciences, 4(2): 295-310. DOI:10.5194/hess-4-295-2000

Nkoue Ndondo, G.R., Probst, J.L., Ndjama, J., Ndam Ngoupayou, J.R., Boeglin, J.L., Takem, G.E., Brunet, F., Mortatti, J., Gauthier-Lafaye, F., Braun, J.J., Ekodeck, G.E., 2021. Stable Carbon Isotopes $\delta^{13}C$ as a Proxy for Characterizing Carbon Sources and Processes in a Small Tropical Headwater Catchment: Nsimi, Cameroon. Aquatic Geochemistry, 27(1): 1-30. DOI:10.1007/s10498-020-09386-8

Norwood, B.S., Stotler, R.L., Brookfield, A., Sullivan, P.L., Macpherson, G.L., 2023. Flux and stable isotope fractionation of CO_2 in a mesic prairie headwater stream. Journal of Water and Climate Change, 14(6): 1961-1976. DOI:10.2166/wcc.2023.067

Noss, C., Bodmer, P., Koca, K., Lorke, A., 2018. Flow and Turbulence driven Water Surface Roughness and Gas Exchange Velocity in Streams. E3S Web of Conferences, 40. DOI:10.1051/e3sconf/20184005018

Öquist, M.G., Wallin, M., Seibert, J., Bishop, K., Laudon, H., 2009. Dissolved Inorganic Carbon Export Across the Soil/Stream Interface and Its Fate in a Boreal Headwater Stream. Environmental Science & Technology, 43(19): 7364-7369. DOI:10.1021/es900416h

Parkhurst, D.L., 1995. User's guide to PHREEQC, a computer program for speciation, reaction-path, advective-transport, and inverse geochemical calculations. 95-4227, Reston, VA. DOI:10.3133/wri954227

Pérez-Rodríguez, M., Biester, H., 2022. Sensitivity of river catchments to discharge-controlled dissolved carbon export: a study of eight catchments in southern Patagonia. Biogeochemistry, 160(2): 177-197. DOI:10.1007/s10533-022-00947-3

Pilla, R.M., Griffiths, N.A., Gu, L., Kao, S.-C., McManamay, R., Ricciuto, D.M., Shi, X., 2022. Anthropogenically driven climate and landscape change effects on inland water carbon dynamics: What have we learned and where are we going? Global Change Biology, 28(19): 5601-5629. DOI:10.1111/gcb.16324

Plummer, L.N., Busenberg, E., 1982. The solubilities of calcite, aragonite and vaterite in CO_2-H_2O solutions between 0 and 90°C, and an evaluation of the aqueous model for the system $CaCO_3$-CO_2-H_2O. Geochimica et Cosmochimica Acta, 46(6): 1011-1040. DOI:10.1016/0016-7037(82)90056-4

Polsenaere, P., Abril, G., 2012. Modelling CO_2 degassing from small acidic rivers using water pCO_2, DIC and $\delta^{13}C$-DIC data. Geochimica et Cosmochimica Acta, 91: 220-239. DOI:10.1016/j.gca.2012.05.030

Potter, B.B., Wimsatt, J.C., 2005. Method 415.3 - Measurement of Total Organic Carbon, Dissolved Organic Carbon and Specific UV Absorbance at 254 nm in Source Water and Drinking Water, Washington, DC. https://www.nemi.gov/methods/method_summary/7228/.

Prijac, A., Gandois, L., Taillardat, P., Bourgault, M.A., Riahi, K., Ponçot, A., Tremblay, A., Garneau, M., 2023. Hydrological connectivity controls dissolved organic carbon exports in a peatland-dominated boreal catchment stream. Hydrology and Earth System Sciences, 27(21): 3935-3955. DOI:10.5194/hess-27-3935-2023

R Core Team Vienna, 2023. R: A language and environment for statistical computing. R Foundation for Statistical Computing, Austria.

Ran, L., Lu, X.X., Liu, S., 2017. Dynamics of riverine CO_2 in the Yangtze River fluvial network and their implications for carbon evasion. Biogeosciences, 14(8): 2183-2198. DOI:10.5194/bg-14-2183-2017

Raymond, P.A., Cole, J.J., 2001. Gas exchange in rivers and estuaries: Choosing a gas transfer velocity. Estuaries, 24(2): 312-317. DOI:10.2307/1352954

Raymond, P.A., Hartmann, J., Lauerwald, R., Sobek, S., McDonald, C., Hoover, M., Butman, D., Striegl, R., Mayorga, E., Humborg, C., Kortelainen, P., Dürr, H., Meybeck, M., Ciais, P., Guth, P., 2013. Global carbon dioxide emissions from inland waters. Nature, 503(7476): 355-359. DOI:10.1038/nature12760

Raymond, P.A., Saiers, J.E., 2010. Event controlled DOC export from forested watersheds. Biogeochemistry, 100(1): 197-209. DOI:10.1007/s10533-010-9416-7

Raymond, P.A., Zappa, C.J., Butman, D., Bott, T.L., Potter, J., Mulholland, P., Laursen, A.E., McDowell, W.H., Newbold, D., 2012. Scaling the gas transfer velocity and hydraulic geometry in streams and small rivers. Limnology and Oceanography: Fluids and Environments, 2(1): 41-53. DOI:10.1215/21573689-1597669

Riise, G., Haaland, S.L., Xiao, Y., 2023. Coupling of iron and dissolved organic matter in lakes–selective retention of different size fractions. Aquatic Sciences, 85(2): 57. DOI:10.1007/s00027-023-00956-w

Rounds, S.A., Wilde, F.D., 2012. Chapter A6. Section 6.6. Alkalinity and acid neutralizing capacity, Reston, VA. DOI:10.3133/twri09A6.6

Sander, M., Hofstetter, T.B., Gorski, C.A., 2015. Electrochemical Analyses of Redox-Active Iron Minerals: A Review of Nonmediated and Mediated Approaches. Environmental Science & Technology, 49(10): 5862-5878. DOI:10.1021/acs.est.5b00006

Schiff, S.L., Aravena, R., Trumbore, S.E., Dillon, P.J., 1990. Dissolved Organic Carbon Cycling in Forested Watersheds: A Carbon Isotope Approach. Water Resources Research, 26(12): 2949-2957. DOI:10.1029/WR026i012p02949

Schimmel, H., Amelung, W., Gottselig, N., Sebastiá, M.-T., Keizer, J.J., Martins, M.A.S., Lohila, A., Müller, C., Laudon, H., Klumpp, E., Braun, M., 2025. Natural Nanoparticles and Colloids in Forested Streams Across Europe: Seasonal Patterns and Impact of Soil Groups. Global Biogeochemical Cycles, 39(6): e2024GB008467. DOI:10.1029/2024GB008467

Schubert, C.M., Juhlke, T.R., Huneau, F., Garel, E., Santoni, S., Barth, J.A.C., van Geldern, R., 2023. An unusual carbon cycle budget of a small stream in a mountain silicate terrain: The case of the Gravona river (Corsica). Ecohydrology, 16(3): e2521. DOI:10.1002/eco.2521

Schubert, C.M., van Geldern, R., Gossel, W., Visser, A.-N., Barth, J.A.C., 2026. Critical assessment of discharge measurements in challenging headwater streams: conventional vs. hot-water injection thermal imaging. Hydrological Sciences Journal: 1-17. DOI:10.1080/02626667.2025.2594631

Shapiro, S.S., Wilk, M.B., 1965. An analysis of variance test for normality (complete samples)†. Biometrika, 52(3-4): 591-611. DOI:10.1093/biomet/52.3-4.591

Škerlep, M., Nehzati, S., Johansson, U., Kleja, D.B., Persson, P., Kritzberg, E.S., 2022. Spruce forest afforestation leading to increased Fe mobilization from soils. Biogeochemistry, 157(3): 273-290. DOI:10.1007/s10533-021-00874-9

Stern, N., Mejia, J., He, S., Yang, Y., Ginder-Vogel, M., Roden, E.E., 2018. Dual role of humic substances as electron donor and shuttle for dissimilatory iron reduction. Environmental Science & Technology, 52(10): 5691-5699. DOI:10.1021/acs.est.7b06574

Swift, R.S., 1996. Organic Matter Characterization, Methods of Soil Analysis. SSSA Book Series, pp. 1011-1069. DOI:10.2136/sssabookser5.3.c35

Tipping, E., Lofts, S., Sonke, J.E., 2011. Humic Ion-Binding Model VII: a revised parameterisation of cation-binding by humic substances. Environmental Chemistry, 8(3): 225-235. DOI:10.1071/EN11016

Tiwari, T., Sponseller, R.A., Laudon, H., 2022. The emerging role of drought as a regulator of dissolved organic carbon in boreal landscapes. Nature Communications, 13(1): 5125. DOI:10.1038/s41467-022-32839-3

Torres-Martínez, J.A., Mora, A., Knappett, P.S.K., Ornelas-Soto, N., Mahlknecht, J., 2020. Tracking nitrate and sulfate sources in groundwater of an urbanized valley using a multi-tracer approach combined with a Bayesian isotope mixing model. Water Research, 182: 115962. DOI:10.1016/j.watres.2020.115962

Ukalska-Jaruga, A., Bejger, R., Debaene, G., Smreczak, B., 2021. Characterization of Soil Organic Matter Individual Fractions (Fulvic Acids, Humic Acids, and Humins) by Spectroscopic and Electrochemical Techniques in Agricultural Soils, Agronomy. DOI:10.3390/agronomy11061067

van Geldern, R., Schulte, P., Mader, M., Baier, A., Barth, J.A.C., 2015. Spatial and temporal variations of pCO_2, dissolved inorganic carbon and stable isotopes along a temperate karstic watercourse. Hydrological Processes, 29(15): 3423-3440. DOI:10.1002/hyp.10457

Wallin, M.B., Audet, J., Peacock, M., Sahlée, E., Winterdahl, M., 2020. Carbon dioxide dynamics in an agricultural headwater stream driven by hydrology and primary production. Biogeosciences, 17(9): 2487-2498. DOI:10.5194/bg-17-2487-2020

Wallin, M.B., Grabs, T., Buffam, I., Laudon, H., Agren, Å., Öquist, M.G., Bishop, K., 2013. Evasion of CO_2 from streams - the dominant component of the carbon export through the aquatic conduit in a boreal landscape. Global Change Biology, 19(3): 785-97. DOI:10.1111/gcb.12083

Wang, F., Tetzlaff, D., Goldhammer, T., Freymueller, J., Soulsby, C., 2025. Hydrological connectivity drives intra- and inter-annual variation in water quality in an intermittent stream network in a mixed land use catchment under drought. Journal of Hydrology, 648: 132420. DOI:10.1016/j.jhydrol.2024.132420

Weishaar, J.L., Aiken, G.R., Bergamaschi, B.A., Fram, M.S., Fujii, R., Mopper, K., 2003. Evaluation of Specific Ultraviolet Absorbance as an Indicator of the Chemical Composition and Reactivity of Dissolved Organic Carbon. Environmental Science & Technology, 37(20): 4702-4708. DOI:10.1021/es030360x

Wilcoxon, F., 1945. Individual Comparisons by Ranking Methods. Biometrics Bulletin, 1(6): 80-83. DOI:10.2307/3001968

Wilkins, M., Sawyer, A., Williams, K., 2016. Seasonal controls on dynamic hyporheic zone redox biogeochemistry, United States. DOI:10.2172/1506963

Winnick, M.J., Saccardi, B., 2024. Impacts of Carbonate Buffering on Atmospheric Equilibration of CO_2, $\delta^{13}C_{DIC}$, and $\delta^{14}C_{DIC}$ in Rivers and Streams. Global Biogeochemical Cycles, 38(2): e2023GB007860. DOI:10.1029/2023GB007860

Yan, Y., Zhang, X., Xu, C., Liu, J., Hu, F., Geng, Z., 2025. Effect of colloidal particle size on physicochemical properties and aggregation behaviors of two alkaline soils. SOIL, 11(1): 85-94. DOI:10.5194/soil-11-85-2025

Zappa, C.J., McGillis, W.R., Raymond, P.A., Edson, J.B., Hintsa, E.J., Zemmelink, H.J., Dacey, J.W.H., Ho, D.T., 2007. Environmental turbulent mixing controls on air-water gas exchange in marine and aquatic systems. Geophysical Research Letters, 34(10): L10601. DOI:10.1029/2006GL028790

Zhang, Z., Furman, A., 2021. Soil redox dynamics under dynamic hydrologic regimes - A review. Science of The Total Environment, 763: 143026. DOI:10.1016/j.scitotenv.2020.143026

Zhao, L., Hong, H., Fang, Q., Hei, H., Algeo, T.J., 2023. Hydrologic regulation of clay-mineral transformations in a redoximorphic soil of subtropical monsoonal China. American Mineralogist, 108(10): 1881-1896. DOI:10.2138/am-2022-8706

Zhong, J., Li, S.L., Tao, F., Yue, F., Liu, C.-Q., 2017. Sensitivity of chemical weathering and dissolved carbon dynamics to hydrological conditions in a typical karst river. Scientific Reports, 7: 42944. DOI:10.1038/srep42944

Zhou, Z., Cartwright, I., 2021. Using geochemistry to identify and quantify the sources, distribution, and fluxes of baseflow to an intermittent river impacted by climate change: The upper Wimmera River, southeast Australia. Science of The Total Environment, 801: 149725. DOI:10.1016/j.scitotenv.2021.149725

Zhou, Z., Cartwright, I., Morgenstern, U., Fifield, L.K., 2024. Integrating major ion geochemistry, stable isotopes (^{18}O, ^{2}H) and radioactive isotopes (^{222}Rn, ^{14}C, ^{36}Cl, ^{3}H) to understand the interaction between catchment waters and an intermittent river. Science of The Total Environment, 908: 167998. DOI:10.1016/j.scitotenv.2023.167998

Supplement Material A – Analytical procedures

S1 Water sample collection

All water samples were taken mid-stream, 0.45 µm filtered (Minisart HighFlow PES, Sartorius AG, Germany), sealed with Parafilm® and stored at 4 °C in a dark environment until analyses took place. The exception were the samples for total alkalinity (TA), that were filled into two 150 ml crimp top clear glass bottles with butyl rubber stoppers for lab titration without prior filtering (CS-Chromatographie Service GmbH, Langerwehe, Germany). Temperature, pH, electrical conductivity (EC), redox potential (Eh) and dissolved oxygen saturation (DO in %) were measured with a WTW Multi 350i instrument (WTW GmbH, Weilheim, Germany) that was calibrated prior to field use. Precisions ranged around ± 0.07 °C for temperature, ± 0.05 for pH, ± 2 % for EC and Eh, and ± 0.42 % for DO. Conductivity values were referenced to 25 °C by a nonlinear correction function for natural waters. Samples for DIC, DOC and their $\delta^{13}C$ isotopes were collected twice per sampling point in pre-poisoned (~50 g L^{-1} saturated $HgCl_2$ solution) 40-ml amber borosilicate glass vials with butyl rubber septa and filled without bubbles. Major ions and trace element samples were collected in 12 mL polypropylene conical centrifuge tubes (Falcon tubes, BD Biosciences, Bedford, USA), whereas samples for $^{18}O/^{16}O$ ratios of dissolved oxygen ($\delta^{18}O_{DO}$) were collected in 12 mL Exetainers™ (LABCO Ltd. Lampeter, U.K). Those exetainers were also pre-poisoned (~25 g L^{-1} saturated $HgCl_2$ solution), filled with a positive meniscus to avoid air bubbles and immediately capped in field using screw caps with a butyl septum. Thus, contamination by atmospheric O_2 was negligible.

S2 Total Alkalinity of water samples

Total alkalinity (TA), defined as the amount of hydrogen ions needed to balance the excess of proton acceptors over donors (Dickson, 1981; Dickson et al., 2007), was measured by laboratory titration using an Eco Titrando titration system (Metrohm AG, Herisau, Switzerland), equipped with a combined pH electrode. Each sample was titrated three times with 0.01 or 0.02 M HCl as titrants, which resulted in relative standard deviations (RSD) of <0.03 mmol L^{-1}. During sampling campaigns 9 (November 2023) to 12 (February 2024), 0.005 M HCl was used instead, as higher concentrations failed to yield results. The titration software performed stepwise acid addition to the 150 mL water sample and automatically determined the inflection point, following the descriptions by Rounds and Wilde (2012). The system was pH calibrated according to the manufacturer's instructions prior to each use.

S3 Stable isotopes and concentrations of water samples

Inorganic carbon stable isotopes ($\delta^{13}C_{DIC}$) and concentrations (DIC) - were analyzed with an automated equilibration unit (Gasbench 2; Thermo Fisher Scientific, Bremen, Germany) coupled in continuous flow mode to a Delta *plus* XP isotope ratio mass spectrometer (Thermo Fisher Scientific, Bremen, Germany). Water samples were transferred from the sample vials using a syringe system and argon gas compensation to prevent CO_2 leakages into pre-acidified (phosphoric acid) helium-flushed 12 mL Labco Exetainers™ (Labco Ltd. Lampeter, U.K). Due to low DIC concentrations of some of the White Main samples, the recommended signal intensity ~6.0 and ~7.5 V (*m/z* 44) (Cheng et al., 2019; van Geldern et al., 2015) could not be achieved in some cases, even after injecting the maximum allowable water volume of 8 mL. This resulted in a small reduction of the typical precision of ± 0.1 ‰. However, the error remained within the limits of ± 0.2 ‰. DIC concentrations were determined from chromatographic peak areas, which are directly proportional to the amount of CO_2 released upon the reaction of the sample with phosphoric acid. A precision of better than 5% was

achieved. More details and information on measurements and data corrections can be viewed in Schubert et al. (2023).

Organic carbon stable isotopes ($\delta^{13}C_{DOC}$) and concentrations (DOC) - Water samples were analyzed for the carbon stable isotope ratio of dissolved organic carbon ($\delta^{13}C_{DOC}$) by an OI Analytical Aurora 1030W TIC-TOC analyzer (OI Analytical, College Station, Texas) coupled in continuous flow mode to a Thermo Scientific Delta V plus isotope ratio mass spectrometer (IRMS). DIC was removed as CO_2 via the addition of 1 mL of 5% phosphoric acid (H_3PO_4) at 70°C for 2 min and the following helium purging. Next 2 mL of 10% sodium persulfate ($Na_2S_2O_8$) were added to the sample and reacted for 5 min at 98 °C to oxidize the DOC to CO_2. This produced CO_2 was again purged from the solution with helium and measured as the analyte gas by the IRMS device. For low concentrations a trap and purge (T & P) system was installed. Details of the coupling of the TIC/TOC analyzer to IRMS are described in St-Jean (2003). Each data set was corrected for instrumental drift and linearity, while carbon isotope values were normalized to the VPDB scale using two laboratory reference materials (C4 sugar and potassium hydrogen phthalate (KHP)) measured in each run. These in-house reference materials were calibrated directly against USGS-40 (L-glutamic acid, -26.39 ‰) and IAEA-CH-6 (sucrose, -10.45 ‰) by using an elemental analyzer (Costech ECS 4010). Precision based on repeated analyses of a control standard (C_3 sugar) during all runs was better than ±0.3 ‰ (1 σ). DOC concentrations were determined using the internal non-dispersive infrared sensor (NDIR) of the OI Aurora 1030W. Calibration was done with a series of standards prepared from analytical (A.C.S.) grade KHP solution of known concentration. The peak area of each sample is directly proportional to the amount of degassed CO_2. Concentration is reported in 10^{-3} mol per liter (mmol L^{-1}). Precision (i.e. reproducibility) was better than 5 % relative standard deviation (RSD).

S4 pCO_2 calculations and error propagation

Partial pressure of carbon dioxide (pCO_2) is taken as an approximation of the gas fugacity of dissolved CO_2, as the difference is <1% under freshwater conditions near-ambient pressure (Dickson et al., 2007). Calculations were based on measured temperature, pH and TA were used with standard carbonate equilibrium formulations (Marx et al., 2017; Plummer and Busenberg, 1982).

$$\mathrm{pCO_2} = \frac{[\mathrm{HCO_3^-}] \times [\mathrm{H^+}]}{\mathrm{K_H} \times \mathrm{K_1}} \tag{A8}$$

where pCO_2 is expressed in µatm, $[HCO_3^-]$ was approximated by TA (mol L^{-1}), $[H^+]$ is 10^{-pH} (dimensionless), K_H is the temperature-dependant Henry's law constant (mol L^{-1} atm^{-1}) and K_1 is the temperature-dependant first dissociation constant of carbonic acid (mol L^{-1}).

Uncertainty in pCO_2 (ΔpCO_2) was assessed by error propagation based on pH (±0.05) and TA (±0.03 mmol L^{-1}) measurements, which represented the dominant sources of error. Temperature errors were neglected. All errors are assumed to be independent and error propagated accordingly for the uncertainty of pCO_2:

$$\frac{\Delta \mathrm{pCO_2}}{\mathrm{pCO_2}} = \sqrt{\left(\frac{\Delta[\mathrm{HCO_3^-}]}{[\mathrm{HCO_3^-}]}\right)^2 + (\ln(10) \times \Delta(\mathrm{pH}))^2} \tag{A2}$$

where $\Delta[HCO_3^-]$ denotes the analytical uncertainty of TA, and $\Delta(pH)$ the instrumental pH measurement error.

S5 F_{CO2} calculations and error propagation

F_{CO2} (mmol m^{-2} d^{-1}) was calculated from the product of the gas transfer velocity k (m d^{-1}) and the concentration difference between dissolved CO_2 in the stream water $[CO_2^*]$ (mmol L^{-1}) and in the water at equilibrium with the overlaying atmosphere $[CO_{2air}]$ (mmol L^{-1}) (Raymond et al., 2012; Schubert et al., 2023; van Geldern et al., 2015):

$$F_{CO_2} = ([CO_2^*]_{water} - [CO_2]_{air}) \times k \quad \text{(A3)}$$

The gas transfer velocity (k) was calculated from stream velocity, based on in-field discharge measurements, and channel slope, following Equation 5, Table 2 in Raymond et al. (2012). $[CO_{2air}]$ was obtained from continuous measurements at the Ochsenkopf station with 90 m elevation (Kubistin et al., 2025), while $[CO_2^*]$ was computed with Equation (56) of Dickson et al. (2007):

$$[\mathrm{CO_2^*}] = \frac{\mathrm{TA} \times [\mathrm{H^+}]^2}{\mathrm{K_1}([\mathrm{H^+}] + 2\mathrm{K_2})} \quad \text{(A4)}$$

Where TA is the total alkalinity (mmol L^{-1}), $[H^+]$ is 10^{-pH}, and K_1 and K_2 are the first and second dissociation constants of carbonic acid.

The uncertainty of ΔCO_2^* was obtained by first-order error propagation, again taking into account the uncertainties of TA and $[H^+]$, while temperature errors are neglected.

$$\Delta\mathrm{CO_2^*} = \sqrt{\left(\frac{[\mathrm{H^+}]^2}{\mathrm{K_1}([\mathrm{H^+}]+2\mathrm{K_2})} \times \Delta\mathrm{TA}\right)^2 + \left(\left[\frac{2\mathrm{TA}[\mathrm{H^+}]}{\mathrm{K_1}([\mathrm{H^+}]+2\mathrm{K_2})} - \frac{\mathrm{TA}[\mathrm{H^+}]^2\mathrm{K_1}}{(\mathrm{K_1}([\mathrm{H^+}]+2\mathrm{K_2})^2}\right] \times \Delta[\mathrm{H^+}]\right)} \quad \text{(A5)}$$

The uncertainty of F_{CO2} was then propagated with the errors of k between 4 and 5%, ΔCO_2^* (Equation 6) and the uncertainty of the atmospheric CO_2 measurements of (0.2 mmol L^{-1}) according to:

$$\Delta F_{CO2} = \sqrt{\left(\left(\left[CO_2^*\right] - [CO_2]_{air}\right) \times \Delta k\right)^2 + \left(k \times \Delta\left[CO_2^*\right]\right)^2 + \left(k \times \Delta[CO_2]_{air}\right)^2} \quad \text{(A6)}$$

All errors were treated as independent, therefore potential covariances were considered negligible during the error propagation.

S6 Major ion analyses and trace elements of water samples

Major cations (Na^+, Mg^{2+}, Ca^{2+}, K^+) and trace elements were analyzed using an iCAP Qc inductively coupled plasma-mass spectrometer (ICP-MS, Thermo Fisher Scientific Inc., Bremen, Germany) equipped with an SC-2DXS autosampler (Elemental Scientifics, Omaha, NV, U.S.A). Each sample was stabilized with two drops of 65 % HNO_3 Suprapur and measured in triplicates, resulting in typical RSD of better than 1 %. The practical quantification limit for most elements was 0.1 µg L^{-1}. Instrumental operating conditions are detailed in Table S1.

Table S1*: ICP-MS operating conditions.*

Plasma Power	1550 W
Cool gas flow	14 L min^{-1}
Auxiliary gas flow	0.65 L min^{-1}
Nebulizer gas flow	1.03 L min^{-1}
CCT (KED mode) flow	5 L min^{-1}
CCT gas	8 % H_2 in He
Sampler/Skimmer	material: Nickel
Spray Chamber Temperature	2.7 °C
Dwell time	10 ms (40ms for Se, As)
Number of Sweeps	70
Sample flow	0.4 ml min^{-1}
LOD typical	< 0.1 ppb

Major anions (F^-, Cl^-, Br^-, NO_3^-, NO_2^-, SO_4^{2-}, PO_4^{3-}) were automatically introduced into the ion chromatography (Compact IC Flex, Metrohm, Herrisau, Switzerland) by autosampler. The method provided a limit of quantification (LOQ) of 0.1 mg L^{-1} with a measurement precision better than 5 % (1σ). Precision was assessed through repeat measurements of two calibration standards, which were treated as unknown samples across both ends of the calibration range.

S7 Ion balance

The ion balance was determined to assess analytical consistency of major cation and anion, as well as trace metal (aluminum, manganese, iron) measurements (Appelo and Postma, 2004; Fritz, 1994):

$$\mathrm{CBE}(\%) = \frac{\sum \text{anions} - \sum \text{cations}}{\sum \text{anions} + \sum \text{cations}} \quad \text{(A7)}$$

Where CBE is given in % and the sum of cations and anions in meq L^{-1}. Negative CBE values suggest excess of cations over anions, while positive values reflect more anions. CBE values of ±5 % are generally considered acceptable (Appelo and Postma, 2004), however, in low-ionic strength waters such as granitic catchments, deviations of up to 10 % are regarded as reasonable (Fritz, 1994). As the CBE exceeded 10% during specific time periods DOC was also added to the sum of anions. Since DOC has no fixed valence, its contribution was roughly estimated from titration experiments on four water samples from M8. Samples were acidified with HCl to pH 4 and then titrated with NaOH to pH >9 to determine the protonation and deprotonation of organic components. The difference between added acid and base was then normalized to the DOC concentration in mol L^{-1} to derive a multiplication factor for including DOC in the ion balance.

S8 Soil sample collection and soil preparation

Soil samples were collected on the 13th of November 2024 from sites M4, M6 and three times at M8 based on its soil heterogeneity at the lowest site. Each sample was homogenized, weighted (wet) and transferred into 50 mL centrifuge tubes (VWR, Avantor Inc., Radnor, PA, USA), which were tightly sealed with Parafilm®. The pore water was extracted by centrifugation at 4700 rpm for 15 minutes using a Heraeus Multifuge L1 (Thermo Fisher Scientific, Waltham, Ma, USA), as centrifugation is recommended for high-precision isotope analysis of extracted pore water (Orlowski et al., 2016). The supernatant was decanted and filtered through 0.45 µm syringe filters (Minisart HighFlow PES, Sartorius AG, Germany) and subsequently analyzed for major ions, tracer elements, carbon concentrations and stable isotope ratios, as well as SUVA and fluorescence analysis. The remaining soil was transferred into aluminum trays and dried at 120 °C using a VWR DRY-Line 112 Prime Drying cabinet (VWR International GmbH, Darmstadt, Germany) for more than 72 h (7 days). The dried soils were sieved to <2 mm.

S9 Mineral abundance (XRD analyses) of soil samples

For the XRD analyses the dried and sieved soil samples were milled with an agate mill in a Vibratory Disc Mill (RS 200, Retsch GmbH, Germany) for ten minutes at 700 min^{-1}. The sample powders were filled into X-ray diffraction sample holders and analyzed using a D5000 X-ray powder diffractometer equipped with a Cu-long-fine-focus tube (Siemens AG, Munich, Germany). The instrument was operated at 40 kV and 35 mA. Scans were conducted from 2 to 65° 2θ with a step size of 0.02° and a counting time of 3 s per step. Mineral abundances were determined semi-quantitatively using the Rietveld algorithm in the Profex software (Doebelin and Kleeberg, 2015).

S10 Size distribution of composite soil sample

The soil sample (a homogenized mixture from M4, M6, and M8) shaken overnight with a dispersing agent (0.05% Sodium Metaphosphate) and then wet sieved to separate the sand fraction from the soil sample (~10 g). The filtrate containing the silt and clay fractions was concentrated in a drying cabinet (80 – 105 °C) and analyzed with the Sedigraph III Plus 5125 coupled to a MasterTech autosampler (Micromeritics Instrument Corporation, Norcoss, GA, USA). The grain size distribution was measured via sedimentation rates calculated with Stoke's law and the particle mass measured directly by X-ray absorption. The boundary between fine sand and coarse silt was set at 50 μm.

S11 Surface charge tested on composite soil samples (Zeta potential)

Zeta potential was measured to assess the surface charge characteristics of suspended soil-derived colloids (He et al., 2021; Hunter, 1981). One composite soil sample was treated with Milli-Q water with a pH of 6.3, similar to that of location M6 to M8 during baseflow conditions, and another with White Main water adjusted to a pH of 4.98, simulating in-situ conditions during high-flow events at site M6 to M8. Samples were shaken for 24 h and centrifuged, after which the supernatant was analyzed using a ZetaView instrument (Particle Metrix GmbH, Inning, Germany, software version 8.0516 SP3) equipped with a 488 nm laser. Measurements were performed at 25 °C without further chemical modification. Particles were tracked via laser scattering microscopy based on electrophoretic mobility (Delgado et al., 2007). Each analysis included 11 camera positions across the cuvette and samples were diluted 1:100 to optimize particle counts at a sensitivity of 80%, ensuring high-quality parabola fitting. The mean zeta potential was calculated from duplicate measurements and reported as the average ± 1 standard deviation.

S12 Extraction of fulvic and humic acids from soil samples

To characterize fractions of NOM, an acid-base extraction with subsequent HCl and NaOH treatments was performed on composite soil material sampled at the White Main (B1). In parallel, to assess naturally mobilized NOM under in-situ conditions, a mild extraction was conducted using only 0.22 µm filtered White Main water (B2) (in SI B, Figure 2). For the acid pre-treatment soil samples were saturated with HCl to remove carbonates and exchangeable cations. This step protonated exchange sites and allowed the extraction of readily soluble fulvic acids (blue-bordered cloud) into the first supernatant (S1). The remaining pellet (P1) was subsequently treated with NaOH (pH > 12), dissolving both humic and more complex fulvic fractions into the second supernatant (S2). Subsamples of S2 were taken for UV-VIS and fluorometric analysis (light blue bordered cloud). A final acidification step (pH<1) allowed the precipitation of humic acids (P3), while fulvic acids remained in the supernatant (S3). This simplified fractionation approach followed the initial steps of the IHSS extraction protocol (International Humic Substances Society, 2024; Swift, 1996) and was also conducted in this form by Krivdin (2024). Purification steps, like dialysis or resin treatments were omitted, as the focus was on general NOM characterization rather than analytical purity.

S13 Spectrophotometric measurements of soil and water samples

UV-VIS measurements **-** Absorbance spectra of NOM fractions were measured using a Tecan Infinite 200Pro microplate reader (Tecan Group Ltd., Männedorf, Switzerland, serial number: 1806012410) in 96-well UV-transparent quartz plates (Hellma QG 96 Well 730.009-44). Spectral scans were conducted over a wavelength range of 200 to 700 nm, in step between 2 nm and 4 nm depending on the measurement batch, with 25 reads per well. Each well was filled with 300 µl of 0.45 µm filtered sample solution. For water samples taken during the flush event, blank correction was performed using MilliQ Water, whereas for soil extracts White Main water

was used instead. In order to calculate the SUVA, all values were normalized to a 1 cm pathlength using a correction factor of 0.871, which corresponds to the effective optical pathlength in the wells based on sample volume and plate geometry (Potter and Wimsatt, 2005). The specific UV absorbance at 254 nm ($SUVA_{254}$) was calculated according to **Equation A8** (Potter and Wimsatt, 2005; Weishaar et al., 2003):

$$SUVA_{254} = \frac{A_{254,\,corr} \times 100}{[DOC]} \quad \text{(A8)}$$

where $A_{254,corr}$ is the pathlength-corrected absorbance, and [DOC] is the dissolved organic carbon concentration in mg C L^{-1}. $SUVA_{254}$ values are reported in L mg C^{-1} m^{-1}. Subsequent fluorescence measurements were conducted as well.

Fluorescence analysis - The UV-VIS measurements were complemented by fluorescence spectra. Therefore, a 96-well UV-transparent quartz plate (Hellma QG 96 Well 730.009-44) was filled with 300 µl sample and measured using the Tecan Infinite 200Pro microplate reader without lid and in top-read mode. Excitation wavelengths ranged from 240 nm to 400 nm with a 4 nm step size, while emission was fixed at 280 nm. Each well was scanned 25 times with a lag time of 0 ms and an integration time of 20 µs. Grain was set to 100 and Z-position was fixed at 20,000 µm. Raw fluorescence intensity values were blank-corrected, and the resulting excitation spectra were used to assess possible composition differences between humic-, fulvic- or protein-like NOM components (Coble, 1996; Levchuk et al., 2018; Mobed et al., 1996).

S14 NMR analysis specifications

^{1}H-NMR and **^{13}C-NMR spectra** were recorded on a Bruker Avance Neo 600 MHz spectrometer equipped with a cryoprobe (CPDCH600S3 C/H-D-05Z). D_2O (Deutero GmbH)

and NaOD (40 wt % in D_2O; Aldrich) were used without further purification. All spectra were measured at 25 °C and are not referenced. ^{1}H-NMR spectra were recorded with water suppression using excitation sculpting (pulprog: zgesgppe). Chemical shifts of the residual HDO signals targeted for suppression were obtained from standard ^{1}H-NMR spectra. ^{13}C-NMR spectra were measured with power-gated proton decoupling (pulprog: zgpg30). Due to the high-quality factor of the probe head a short pre-scan delay of 25 µsec was used. Despite this, spectra exhibited pronounced baseline roll and automatic baseline correction was inadequate due to broad peaks. For this reason, we applied combinations of sine and polynominal functions and cubic splines (Details given in Table S2).

Table S2*: Spectrum-specific measurement and post-processing parameters.*

Sample	**Sample amount [mg]**	**Nucleus**	**Number of scans**	**Recovery delay [s]**	**Baseline correction**	**Line broadening [Hz]**
HSS-Pahokee	20	1H	32	2	Sine + polynominal functions, cubic splines	10
HSS-Pahokee	20	13C	192000	0.1	Sine + polynominal functions, cubic splines	10
B2	73	1H	32	2	Sine + polynominal	0.3

					functions, cubic splines	
B2	73	13C	288000	0.1	cubic spline	1
S1 B1	93	13C	420840	0.1	Sine + polynominal functions, cubic splines	5
S3.1/3.2 B1	70	13C	544574	0.1	Sine + polynominal functions, cubic splines	5
P3.2/P3.1 B1	not determined	1H	32	2	-	0.3
P3.2/P3.1 B1	not determined	13C	99240	0.1	Sine + polynominal functions, cubic splines	5

S15 Isotopic two-component source partitioning

To determine the fractional contribution of DOC-derived carbon versus degassing-influenced DIC on the observed $\delta^{13}C_{DIC}$ signal, a two-member isotope mixing approach was applied (Kendall and Caldwell, 1998), assuming that the contributions from the two sources sum to one ($f_A + f_B = 1$).

$$\delta_{mix} = (\delta_A \times f_A) + (\delta_B \times f_B) \quad \text{(A9)}$$

$$f_A = \frac{\delta_{mix} - \delta_B}{\delta_A - \delta_B} \quad \text{(A10)}$$

$$f_B = \frac{\delta_A - \delta_{mix}}{\delta_A - \delta_B} \quad \text{(A11)}$$

Here, f_A is the fraction of carbon in DIC originating from DOC, while f_B is the fraction of DIC originating from degassing influence. δ_{mix} is the measured $\delta^{13}C_{DIC}$ at each site and flow condition. δ_A is the isotopic signature of DOC (component A), defined as the site-specific mean $\delta^{13}C_{DOC}$ measured under either baseflow or high flow conditions. δ_B is the isotopic signature of the DIC component influenced by degassing (component B), derived from LOESS regression fits of $\delta^{13}C_{DIC}$ plotted against DIC concentrations during baseflow as it was assumed that the degassing component was dominant while component A could be neglected (SI B, Figure S8). The baseflow-LOESS fit was generated in R and used to interpolate δ_B at the respective DIC concentrations, averaged by site.

References

Appelo, C.A.J., Postma, D., 2004. Geochemistry, Groundwater and Pollution (2nd ed.). CRC Press, London. DOI:10.1201/9781439833544

Cheng, L. et al., 2019. An international intercomparison of stable carbon isotope composition measurements of dissolved inorganic carbon in seawater. Limnology and Oceanography: Methods, 17(3), 200-209. DOI:10.1002/lom3.10300

Coble, P.G., 1996. Characterization of marine and terrestrial DOM in seawater using excitation-emission matrix spectroscopy. Marine Chemistry, 51(4): 325-346. DOI:10.1016/0304-4203(95)00062-3

Delgado, A.V., González-Caballero, F., Hunter, R.J., Koopal, L.K., Lyklema, J., 2007. Measurement and interpretation of electrokinetic phenomena. Journal of Colloid and Interface Science, 309(2), 194-224. DOI:10.1016/j.jcis.2006.12.075

Dickson, A.G., 1981. An exact definition of total alkalinity and a procedure for the estimation of alkalinity and total inorganic carbon from titration data. Deep Sea Research Part A. Oceanographic Research Papers, 28(6), 609-623. DOI:10.1016/0198-0149(81)90121-7

Dickson, A.G., Sabine, C.L., Christian, J.R., 2007. Guide to best practices for ocean CO_2 measurements. PICES Special Publication, pp. 191, Accessible at: http://www.cdiac.ornl.gov/oceans/Handbook_2007.html.

Doebelin, N., Kleeberg, R., 2015. Profex: A graphical user interface for the Rietveld refinement program BGMN. Journal of Applied Crystallography, 48, 1573-1580. DOI:10.1107/S1600576715014685

Fritz, S.J., 1994. A Survey of Charge-Balance Errors on Published Analyses of Potable Ground and Surface Waters. Groundwater, 32(4), 539-546. DOI:https://doi.org/10.1111/j.1745-6584.1994.tb00888.x

He, Y., Yang, M., Huang, R., Wang, Y., Ali, W., 2021. Soil organic matter and clay zeta potential influence aggregation of a clayey red soil (Ultisol) under long-term fertilization. Scientific Reports, 11(1), 20498. DOI:10.1038/s41598-021-99769-w

Hunter, R.J., 1981. Zeta Potential in Colloid Science: Principles and Applications. Academic Press, London. DOI:10.1016/C2013-0-07389-6

International Humic Substances Society, 2024. Isolation of IHSS Soil Fulvic and Humic Acids. Accessible at: https://humic-substances.org/ [Accessed on 14th of July 2025].

Kendall, C., Caldwell, E.A., 1998. Chapter 2 - Fundamentals of Isotope Geochemistry. In: Kendall, C., McDonnell, J.J. (Eds.), Isotope Tracers in Catchment Hydrology. Elsevier, Amsterdam, pp. 51-86. DOI:https://doi.org/10.1016/B978-0-444-81546-0.50009-4

Krivdin, Leonid B., 2024. Liquid-Phase NMR of Humic and Fulvic Acids. Magnetic Resonance in Chemistry, 63(2), 128-150. DOI:10.1002/mrc.5493

Kubistin, D. et al., 2025. ICOS ATC NRT CO2 growing time series from Ochsenkopf (90.0 m). In: Centre, A.T. (Ed.), Accessible at: https://hdl.handle.net/11676/1jylHIBnJMssyniOEKk34cd3 [Accessed on 29th of July 2025].

Levchuk, I., Rueda Márquez, J.J., Sillanpää, M., 2018. Removal of natural organic matter (NOM) from water by ion exchange – A review. Chemosphere, 192, 90-104. DOI:10.1016/j.chemosphere.2017.10.101

Maier, J., Visser, A.N., Schubert, C.M., Wander, S.T., Barth, J.A., 2025. Hydrodynamic and Primary Production Effects on Seasonal DO Variability in the Danube River. EGUsphere, 2025, 1-25. DOI:10.5194/egusphere-2025-1580

Marx, A. et al., 2017. A review of CO2 and associated carbon dynamics in headwater streams: A global perspective. Reviews of Geophysics, 55(2): 560-585. DOI:10.1002/2016RG000547

Mobed, J.J., Hemmingsen, S.L., Autry, J.L., McGown, L.B., 1996. Fluorescence Characterization of IHSS Humic Substances: Total Luminescence Spectra with Absorbance Correction. Environmental Science & Technology, 30(10), 3061-3065. DOI:10.1021/es960132l

Orlowski, N., Pratt, D.L., McDonnell, J.J., 2016. Intercomparison of soil pore water extraction methods for stable isotope analysis. Hydrological Processes, 30(19), 3434-3449. DOI:10.1002/hyp.10870

Plummer, L.N., Busenberg, E., 1982. The solubilities of calcite, aragonite and vaterite in CO_2-H_2O solutions between 0 and 90°C, and an evaluation of the aqueous model for the system $CaCO_3$-CO_2-H_2O. Geochimica et Cosmochimica Acta, 46(6), 1011-1040. DOI:10.1016/0016-7037(82)90056-4

Potter, B.B., Wimsatt, J.C., 2005. Method 415.3 - Measurement of Total Organic Carbon, Dissolved Organic Carbon and Specific UV Absorbance at 254 nm in Source Water and Drinking Water, Washington, DC. https://cfpub.epa.gov.

Raymond, P.A. et al., 2012. Scaling the gas transfer velocity and hydraulic geometry in streams and small rivers. Limnology and Oceanography: Fluids and Environments, 2(1), 41-53. DOI:10.1215/21573689-1597669

Rounds, S.A., Wilde, F.D., 2012. Chapter A6. Section 6.6. Alkalinity and acid neutralizing capacity, Reston, VA. DOI:10.3133/twri09A6.6

Schubert, C.M. et al., 2023. An unusual carbon cycle budget of a small stream in a mountain silicate terrain: The case of the Gravona river (Corsica). Ecohydrology, 16(3), e2521. DOI:10.1002/eco.2521

St-Jean, G., 2003. Automated quantitative and isotopic (^{13}C) analysis of dissolved inorganic carbon and dissolved organic carbon in continuous-flow using a total organic carbon analyser. Rapid Communications in Mass Spectrometry, 17(5), 419-428. DOI:10.1002/rcm.926

Swift, R.S., 1996. Organic Matter Characterization, Methods of Soil Analysis. SSSA Book Series, pp. 1011-1069. DOI:10.2136/sssabookser5.3.c35

van Geldern, R., Schulte, P., Mader, M., Baier, A., Barth, J.A.C., 2015. Spatial and temporal variations of pCO2, dissolved inorganic carbon and stable isotopes along a temperate karstic watercourse. Hydrological Processes, 29(15), 3423-3440. DOI:10.1002/hyp.10457

Weishaar, J.L. et al., 2003. Evaluation of Specific Ultraviolet Absorbance as an Indicator of the Chemical Composition and Reactivity of Dissolved Organic Carbon. Environmental Science & Technology, 37(20), 4702-4708. DOI:10.1021/es030360x

Supporting information B

I. Figures

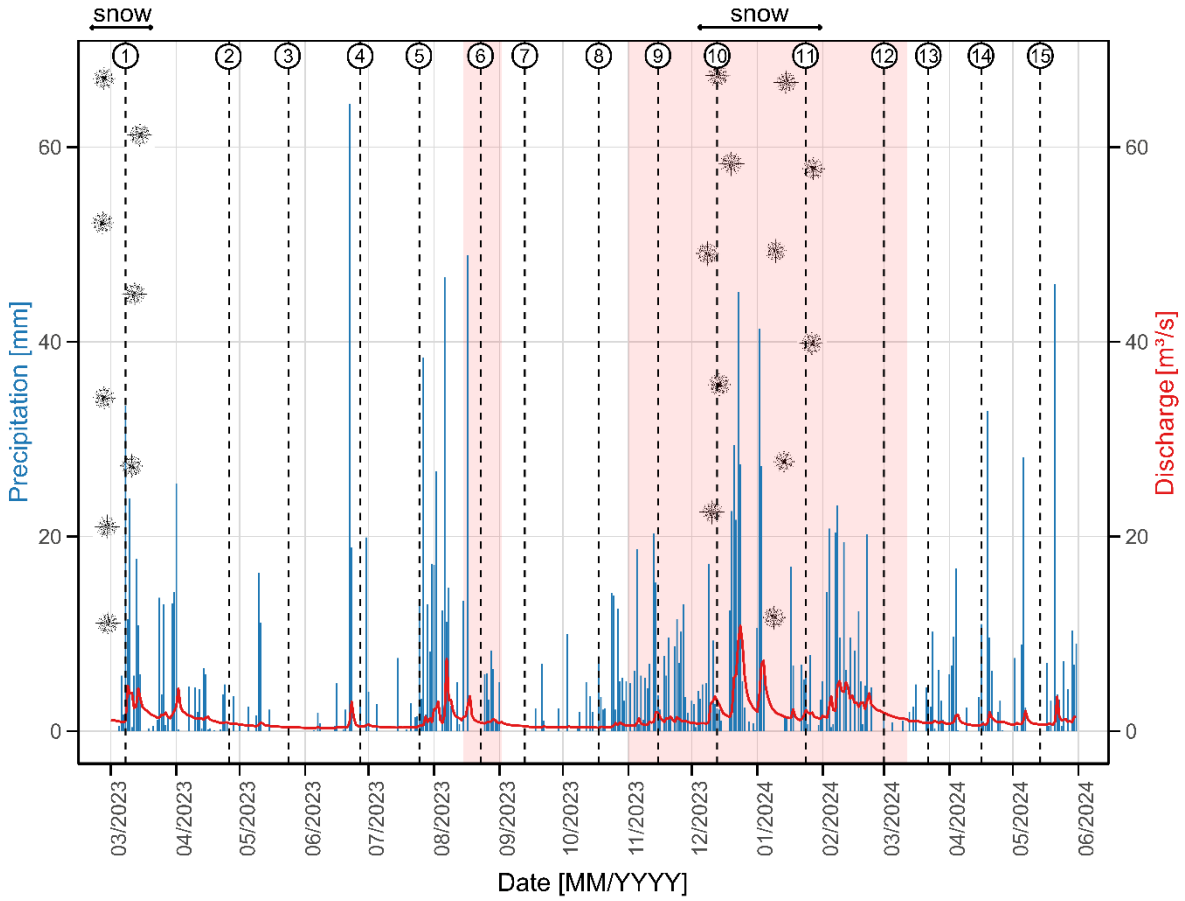

Figure S1: Precipitation in mm (DWD, station Bischofsgrün, dark blue bars) and discharge in $m^3\ s^{-1}$ (GKD Bayern, station Bad Berneck, red line) over the whole sampling period. Sampling events in the White Main headwater catchment are indicated by numbers from 1 to 15 and dotted vertical lines. Periods of snow cover are marked with black arrows and labelled as snow in the upper part of the graph. Pink shaded areas indicate times of high discharge that coincide with episodes of increased hydrochemical variability.

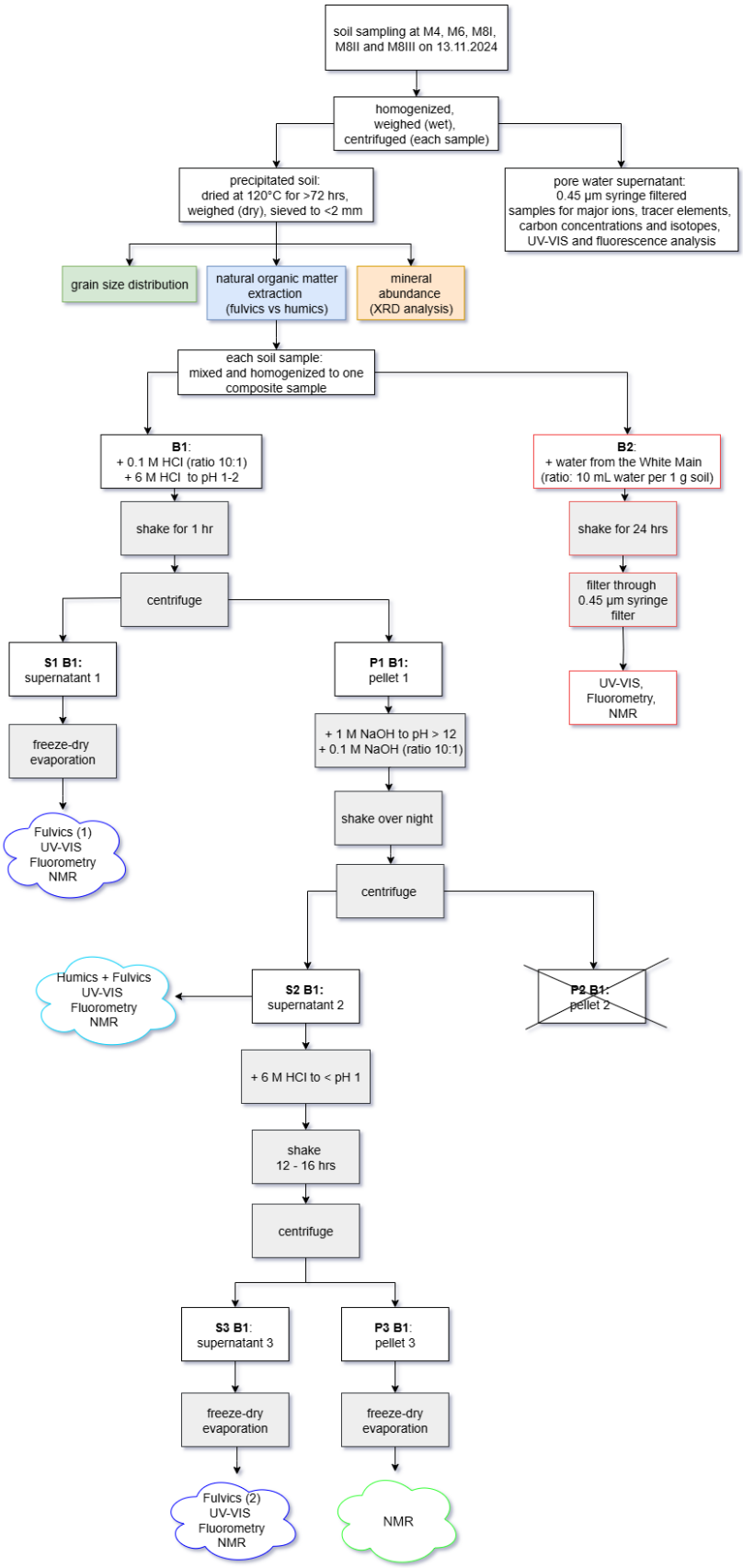

Figure S2: Flow chart summarizing soil sampling and processing for grain size distribution and XRD measurements, as well as natural organic matter (NOM) extraction applied to the samples from sites M4, M6, M8I-III. Full descriptions of the soil extracts can be viewed in SI A, S12.

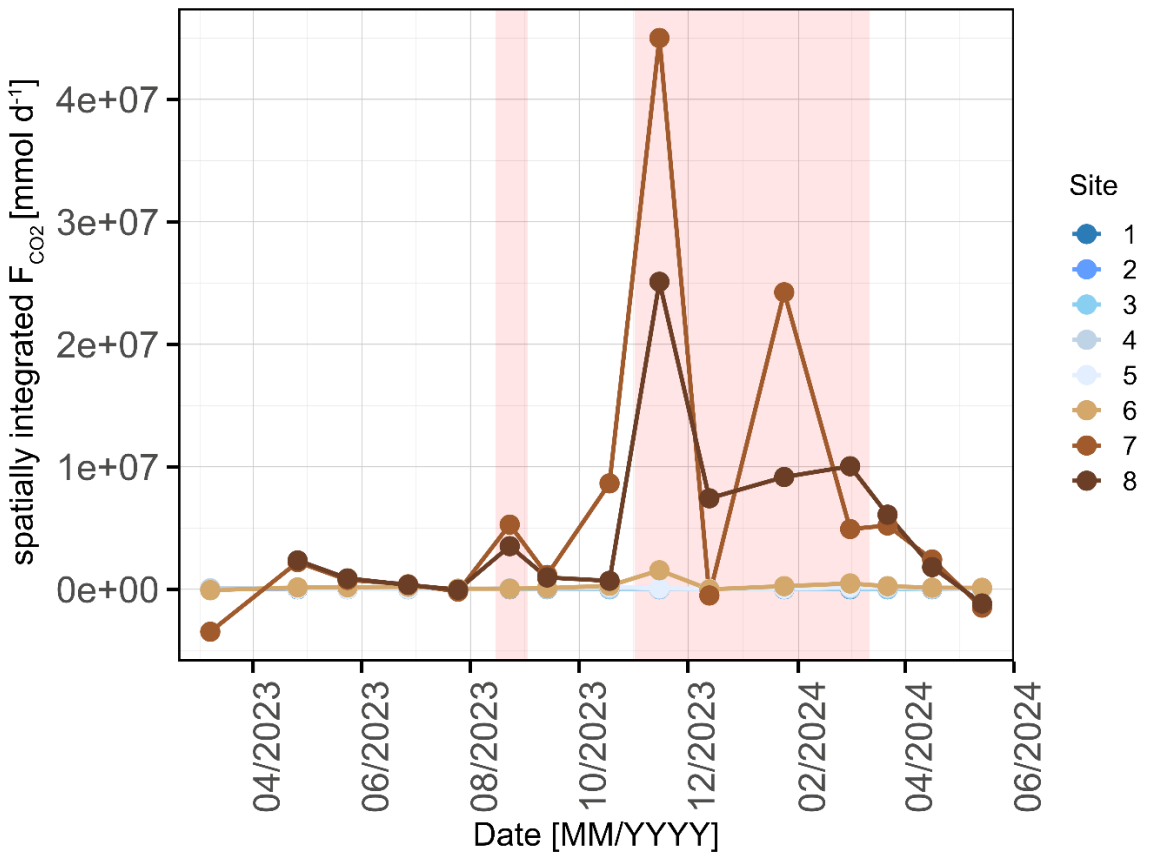

Figure S3: Spatially integrated F_{CO2}, representing the sum of CO_2 fluxes from all sampling points normalized to the respective rive surface area from Marh 2023 to August 2024. Red shaded areas indicate times of high discharge. No errors were determined.

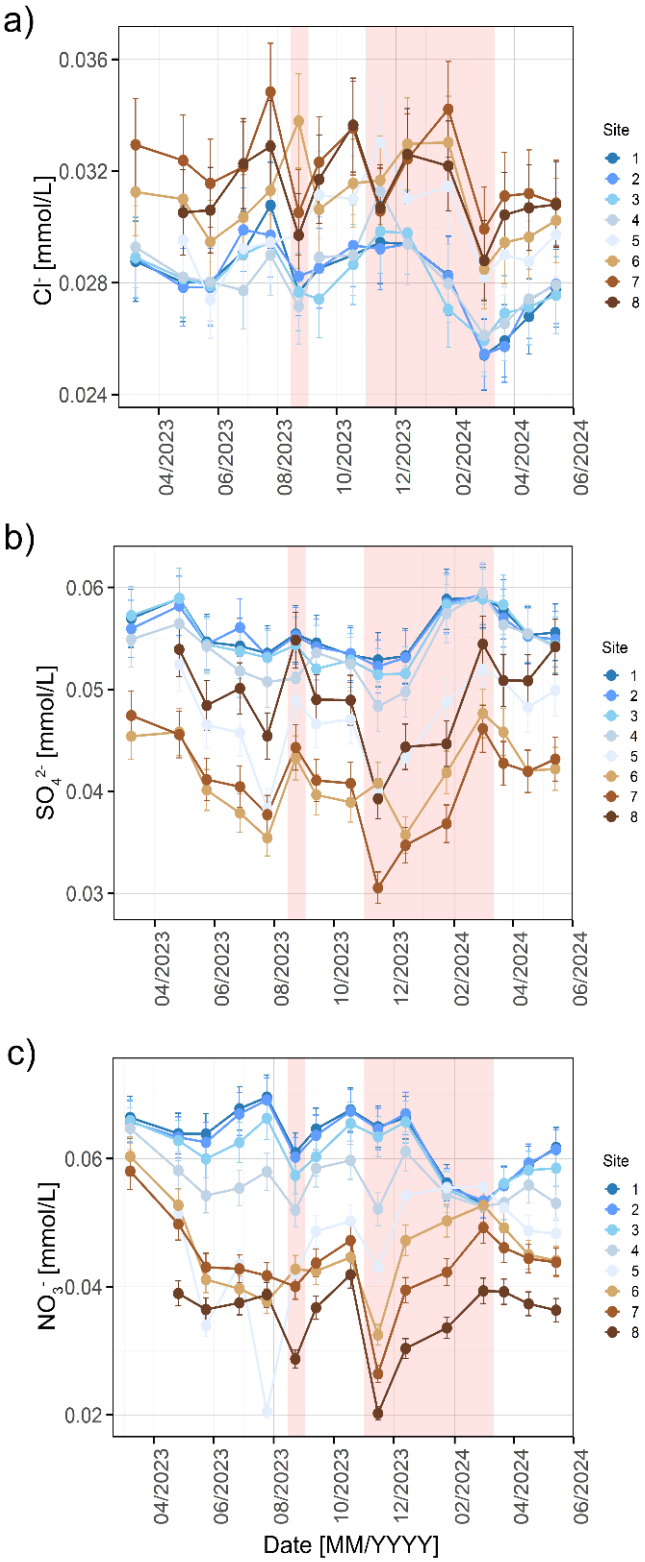

Figure S4: Temporal evolution of a) chloride (Cl^-), b) sulfate (SO_4^{2-}), and c) nitrate (NO_3^-) concentrations (mmol L^{-1}) along the eight White Main sampling points from March 2023 to June 2024. Shaded red areas indicate periods of high discharge.

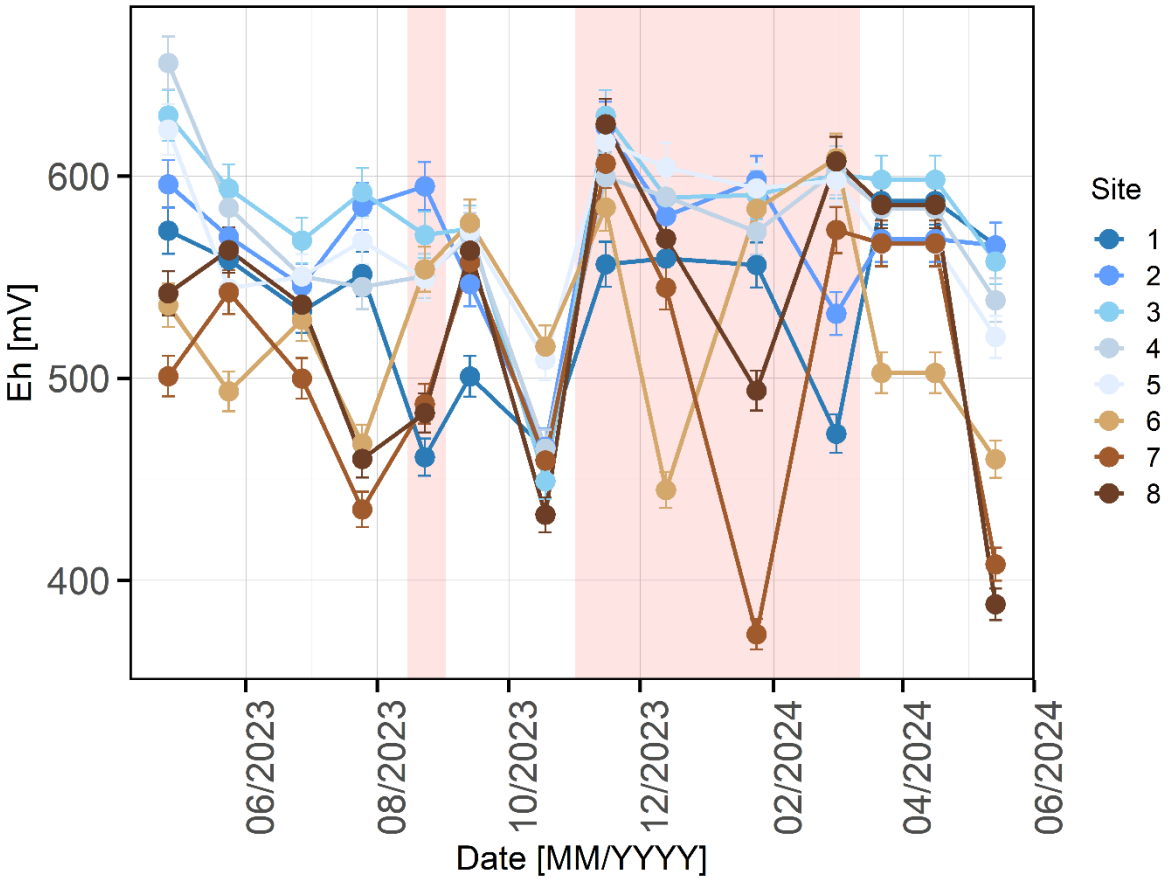

Figure S5: Temporal evolution of redox potential (Eh, mV) at the eight sampling locations between May 2023 to June 2024. Shaded red areas denote times of high discharge.

a)  b) 

Figure S6: a) Water browning during high flow in the stream at site M8 and b) in the sampling water buckets.

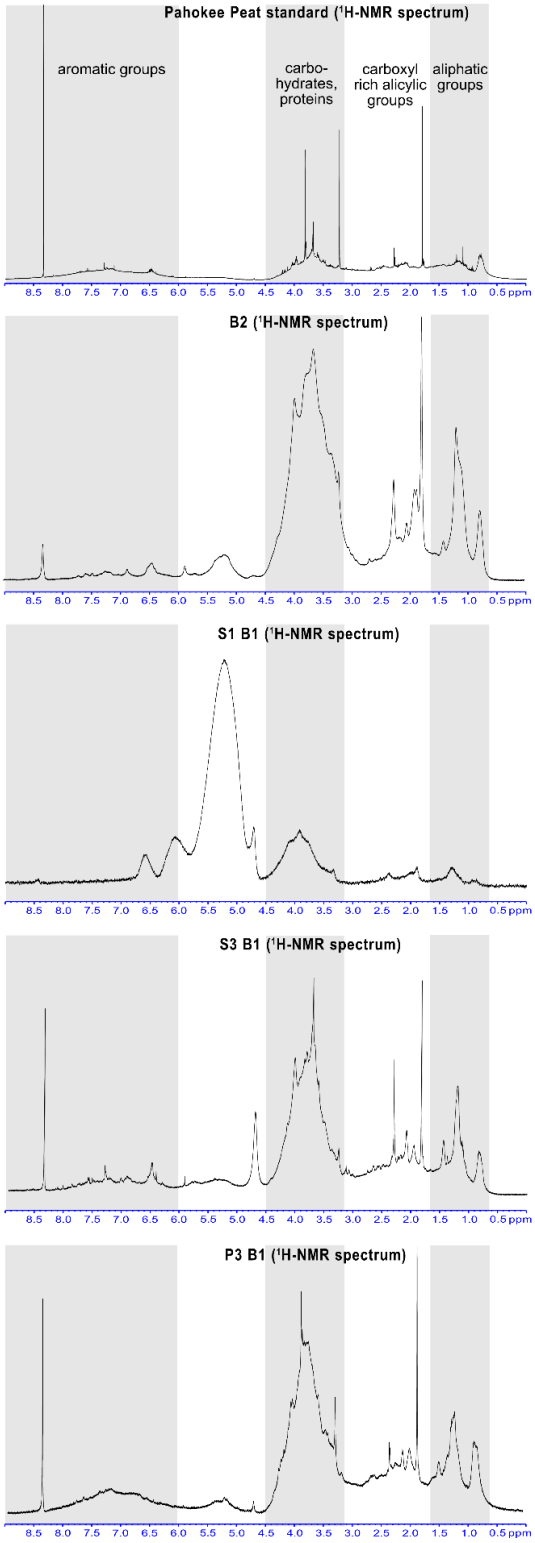

Figure S7: ^{1}H-NMR spectra of soil extract fractions (B2, S1-B1 to S3-B1, P3 B1, see Supplementary material B, Figure 2) compared to the Pahokee Peat standard (PPHA). Grey-shaded and white areas indicate the major carbon functional group ranges. Further details on the measurement method are available in SI A, S14.

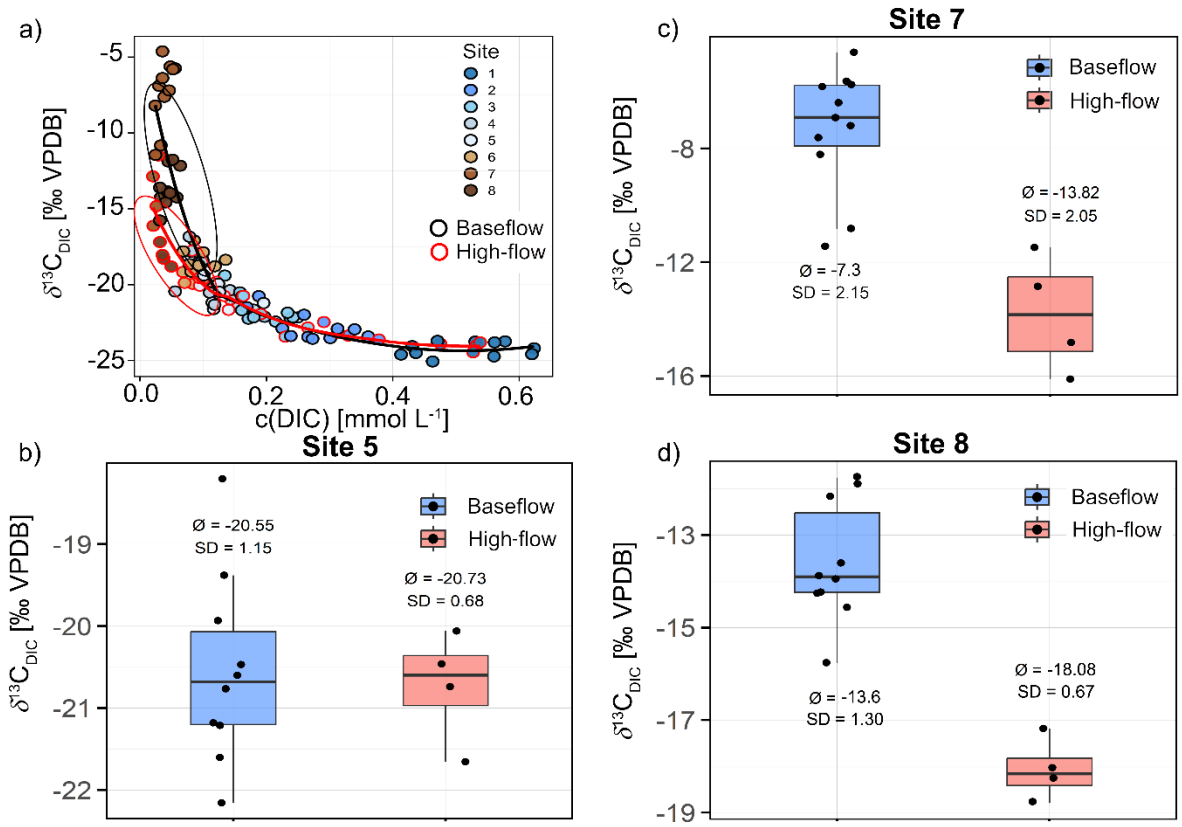

Figure S8: a) Relationship between dissolved inorganic carbon (DIC, mmol L^{-1}) and $\delta^{13}C_{DIC}$ (‰ VPDB) across all eight sampling locations and all sampling times. Samples collected under baseflow conditions are shown with black contours, while high-flow conditions show red contours. b) to d) Boxplots illustrating site-specific variability for high- (red) and baseflow conditions (blue) at site 5, 7 and 8. Mean values (Ø) and standard deviations (SD) are indicated above or below each boxplot.

II. Tables

Table S1: Summary of pH after 24 h shaking, zeta potential, particle concentrations and EC measured in soil samples from sites M4, M6 and M8I-III prepared with Milli-Q and WMQ (White Main) water (A). The table also includes statistical test results (Shapiro-Wilk, Levene, ANOVA and Wilcox) for comparison between the two water treatments (B) and among soil samples (C).

ph of Milli-Q				6.28		
pH of WMQ water (M4, M6, M8I-III)				5.92		
	sample	pH after 24 h (-)	Zeta potential (mV) 1:100	Zeta potential (mV) 1:1	Concentration (particles per ml)	EC ($\mu S\ cm^{-1}$)
+ Milli-Q water	M4	3.99	-18.6365	-10.116	2.68E+09	3.70E+01
	M6	4.00	-24.0395	-21.503	9.80E+08	1.55E+01
	M8I	3.75	-13.886	-18.2355	5.75E+08	2.03E+01
	M8II	3.87	-15.815		1.85E+07	7.53E+01
	M8III	4.38		-2.93	2.00E+05	9.58E+01
+ WMQ water	M4	4.01	-18.85		7.00E+01	9.60E+09
	M6	3.93	-23.293		7.23E+01	6.40E+09
	M8I	3.76	-21.321		6.80E+01	6.40E+09
	M8II	3.85	-20.524		6.58E+01	5.95E+09

	M8III	4.35		-1.539	1.45E+02	2.00E+05
	WMQ water			-22.103	5.78E+01	5.35E+05

(B)

Parameters	Shapiro_ Milli-Q_p	Shapiro_ WMQ_p	Levene_p	ANOVA_p	Wilcox_p	Significant?
pH (after 24 h)	0.43757231	0.42373796	0.98505737	**0.905269**	1	No
Zeta potential [mV]	0.73577962	0.01675066	0.94092697	0.708276	**0.53086930**	No
Concentration [particles per mL]	0.15201140	0.24294223	0.35248843	**0.018561**	0.11496100	Yes
Conductivity [µS/cm]	0.37401043	0.00116589	0.57724126	0.144572	**0.40339531**	No

(C)

Parameters	Shapiro_ Wilk	Levene_p	ANOVA_p	Wilcox_p	Significant?
pH (after 24 h)	0.2471	0.069629743	**0.000301**	0.050186	Yes

Zeta potential	0.8261	0.182458061	**0.00016**	0.050186	Yes
Concentration [particles per mL]	0.3179	0.017162164	0.152697	**0.048798**	Yes
Electrical conductivity [µS/cm]	0.0288	0.693559849	**0.011602**	0.050186	Yes

Table S2: Table of the total sum (across the whole sampling transect) of spatially integrated F_{CO2} values for each sampled month. Bold months are high-flow times. Red values indicate negative fluxes.

Sampling month	Total sum of the spatially integrated F_{CO2} [mmol d^{-1}]
March 2023	-3.4E+06
April 2023	4.9E+06
May 2023	1.9E+06
June 2023	1.1E+06
July 2023	-1.3E+05
August 2023	9.0E+06
September 2023	2.4E+06

October 2023	9.9E+06
November 2023	7.2E+07
Deceber 2023	7.0E+06
January 2024	3.4E+07
February 2024	1.6E+07
March 2024	1.2E+07
April 2024	4.5E+06
May 2024	-2.4E+06

Baseflow average: 3.08E+06

High flow average: 2.75E+07

Table S3: Summary of two-endmember isotope mass-balance calculations for DOC-derived and DIC derived CO_2 at sites M5-M8 under baseflow and high flow conditions. δ_A represents the measured $\delta^{13}C_{DOC}$, δ_B the $\delta^{13}C_{DIC}$, predicted from the degassing trend. δ_{mix} is the measured $\delta^{13}C_{DIC}$ and F_A and F_B the calculated fractional contributions of DOC-derived and DIC-derived CO_2. The mass-balance at M7 during baseflow likely failed with a CO_2 contribution of 121% from $\delta^{13}C_{DIC}$ due to violations of isotopic steady-state assumptions under intense forced degassing at the small waterfall.

Sites		**δ_A (DOC)**	**δ_B (degassing)**	**δ_{mix}**	**f_A**	**f_B**
5	high flow	-27.9	-20.4	-20.73	4%	96%
	baseflow	-27.9	-20.4	-20.55	2%	98%
6	high flow	-27.8	-18	-19.65	17%	83%
	baseflow	-27.1	-18	-18.28	3%	97%
7	high flow	-27.3	-10.7	-13.82	19%	81%
	baseflow	-27.1	-10.7	-7.3	-21%	121%
8	high flow	-27.4	-11.7	-18.08	41%	59%
	baseflow	-27.8	-11.7	-13.6	12%	88%